Theoretical Performance of MOSFET with Graphene Channel

by

Md. Tawabur Rahman

A thesis submitted in partial fulfillment of the requirements for the degree of Master of Science in Electrical and Electronic Engineering

Department of Electrical and Electronic Engineering
Khulna University of Engineering & Technology
Khulna 920300, Bangladesh
June 2014

Declaration

This is to certify that the thesis work entitled *"Theoretical Performance of MOSFET with Graphene Channel"* has been carried out by *Md. Tawabur Rahman* in the Department of *Electrical and Electronic Engineering*, Khulna University of Engineering & Technology, Khulna, Bangladesh. The above thesis work or any part of this work has not been submitted anywhere for the award of any degree or diploma.
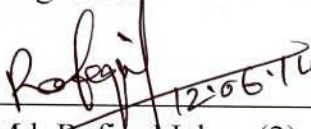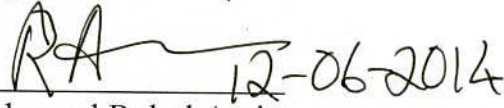

Signature of Supervisor   Signature of Candidate

Approval

This is to certify that the thesis work submitted by *Md. Tawabur Rahman* entitled *"Theoretical Performance of MOSFET with Graphene Channel"* has been approved by the board of examiners for the partial fulfillment of the requirements for the degree of *M. Sc. Engineering* in the Department of *Electrical and Electronic Engineering*, Khulna University of Engineering & Technology, Khulna, Bangladesh in June 2014.

BOARD OF EXAMINERS

1. _____

   12.06.2014

   Prof. Dr. Ashraful Ghani Bhuiyan
   Dept. of Electrical and Electronic Engineering
   Khulna University of Engineering & Technology
   Khulna, Bangladesh

   Chairman
   (Supervisor)

2. _____

   12.06.14

   Head of the Department
   Dept. of Electrical and Electronic Engineering
   Khulna University of Engineering & Technology
   Khulna, Bangladesh

   Member

3. _____

   12.6.14

   Prof. Dr. Md. Rafiqul Islam (1)
   Dept. of Electrical and Electronic Engineering
   Khulna University of Engineering & Technology
   Khulna, Bangladesh

   Member

4. _____

   12.06.14

   Prof. Dr. Md. Rafiqul Islam (2)
   Dept. of Electrical and Electronic Engineering
   Khulna University of Engineering & Technology
   Khulna, Bangladesh

   Member

5. _____

   12-06-2014

   Prof. Dr. Mohamed Ruhul Amin
   Dept. of Electronics & Communications Engineering
   East West University
   Dhaka, Bangladesh

   Member
   (External)

Acknowledgement

It is a great pleasure for me to express unbound indebted gratitude to my supervisor Dr. Ashraful Ghani Bhuiyan, Professor, Department of Electrical and Electronic Engineering of Khulna University of Engineering & Technology, for his numerous helpful & constructive suggestions, scholastic guidance, constant inspiration & support, valuable advice and kind co-operation for the successful completion of work *"Theoretical Performance of MOSFET with Graphene Channel"*. He has always been extremely generous with his time, knowledge and ideas and allowed me great freedom in this research. His enthusiastic approach and endless excitement to research and effervescent personality have made this thesis all the more enjoyable and I am greatly encouraged.

I would also like to thank my family and friends for their continuous encouragement and moral support.

Author

ABSTRACT

The electronics components are becoming progressively smaller, gate scaling process has become saturated and the limits to Moore's Law are frequently considered. To overcome the difficulties of downscaling problems new structures and materials have been studied. The discovery of graphene has gained tremendous attention as the most promising materials for high speed electronic devices. Graphene, a flat mono layer of sp^2 carbon atoms tightly packed into a two-dimensional (2D) honeycomb lattice, has recently attracted broad attention for future electronic device applications because of their excellent electronic characteristics such as high carrier mobility and high saturation velocity. The novel electronic properties of graphene lead to intense research into possible applications of this material in field effect transistors and nano scale devices.

In this thesis, the performance of a graphene MOSFET is analyzed in large area and ballistic limit. The performance of a dual-gated large area graphene MOSFET is analyzed using analytical approach. The quantum transport simulation based on the NEGF formalism is used to analyze the performance of a top-gated graphene MOSFET in ballistic limit. The NEGF formalism is self-consistently coupled to the 1D Poisson equations. The Poisson equation is solved in 1D coordinate using the finite difference method (FDM).

In large area dual gate graphene MOSFET, we have calculated sheet charge density dependent quantum capacitance self consistently considering charged impurities in the gate oxide layer. It is observed that with increasing. It is observed that with increasing charged impurities concentration the quantum capacitance increases near the Dirac point due to the limited density of states.With increasing the value of impurities concentration in the gate oxide layer,the minimum value of the quantum capacitance is also increased. Ultimately quantum capacitance is controlling the gate capacitance as well as the sheet charge density of graphene channel.

A quasi-saturation of drain current called "kink" is observed in the output characteristics of both in large area and ballistic graphene MOSFET. This behaviour occurs due to the ambipolar nature of graphene channel. An ambipolar behavior occurs for a change in the conduction type at the drain end of the channel from p-type to n-type is clearly shown in transfer characteristics. Such a behavior is specific for G-MOSFETs, caused by the gapless nature of the channel due to the zero bandgap, and does not occur in conventional field effect transistors.

The variation of sheet charge density with channel length at different drain bias (V_{ds}) is also shown. As V_{ds} is decreased negatively the corresponding sheet charge density decreases up to dirac point. After dirac point we obtain a positive gate to channel voltage at drain end which gives rise to an accumulation of electrons and corresponding increase in sheet charge density. The carrier drift velocity is increasing linearly with electric field

but at a electric field of E=75.06 kV/cm, carrier drift velocity saturates to the average Fermi velocity of $2.12 \times 10^7 cms^{-1}$.

In ballistic graphene MOSFET, The I-V characteristics shows standard MOSFET type behavior along with the high drain current current density reaching to approximately 12,000 $\mu A/\mu m$ which is promising. The reason for the high current density can be attributed to the light effective mass of graphene and high carrier velocity. At lower gate voltage, a pronounced 'kink' is observed in drain current characteristics. At higher gate voltage this 'kink' behavior almost disappears. With the help of transfer characteristics, it is noticed that the dirac point shifts when the drain-source voltage is varied. The dirac point voltage, V_{dirac} shifts significantly towards right at positive drain bias where as V_{dirac} shifts slightly towards left at negative drain bias. Therefore, the shift of dirac point voltage V_{dirac} in positive drain bias is more prominent than negative drain bias. Also, the p-n assymetry in transfer characteristics is the signature of short channel effect.

The output transconductance of the device is obtained in the range of = 4500 $\mu S/um$ which is very much promising for high speed nano transistors. The variation of output transconductance, g_m with the channel length is also shown. It is found that drain transconductance decreases at longer channel length. But, as the channel length scales down to 50 nm, the drain transconductance (g_{ds}) rises significantly due to electrostatic gate effect.

Contents

List of Figures

Figure No.	Figure Title	Page No.
1.1	A schematic showing the high quality large domain graphene by advanced synthesis method along with the current and future applications.	02
2.1	(a) Graphene is an atomic-scale honeycomb lattice made of carbon atoms (b) SEM micrograph of a strongly crumpled graphene sheet on a Si wafer (Online)	04
2.2	(a) The unit cell of the graphene real-space lattice is colored in green. (b) Displayed is the first Brillouin zone with the position of each K-point.	06
2.3	(a) The band structure of graphene is displayed. The valance band is colored in orange and the conduction band is colored in blue. (b) A magnified section around the K-point is shown.	06
3.1	The cross section of the modeled graphene MOSFET with top- and back-gate.	12
3.2	Fermi energy in undopedgraphene for zero gate and drain-source voltage	14
3.3	The energy bands are down-shifted with respect to the Fermi energy if a positive gate voltage is applied.	15
3.4	Equivalent capacitive circuit of a graphene MOSFET with both top-gate and back-gate.	22
3.5	The cross section of the discretized Graphene channel	24
3.6	Cross section of the modeled top gate-graphene MOSFET	28
3.7	(a) A device driven out of equilibrium by two contacts with different Fermi levels μ_1 and μ_2 (b) Self-consistent procedure for determining the density matrix from which all quantities of interest (electron density, current etc.) can be calculated.	29-30
3.8	The interaction of a device with a reservoir can be represented by a self-energy matrix Σ	31
3.9	A discrete level is coupled to a reservoir with a Fermi level μ. The broadening is the same regardless of whether the reservoir states are empty or filled. (a) Level coupled to empty states (b) level coupled to filled states.	35
3.10	The eigenstates of a composite contact–device–contact structure can be divided into two groups associated with incident waves from the (A) left contact (B) the right contact.	35

List of Tables

Nomenclature

Symbol	Unit	Description
a_0	cm	Carbon-carbon distance
α	eV	Self-energy
β	eV	Hopping energy between nearest neighbors
δ	dimensionless	Delta function
ϕ	dimensionless	Electron wave function of the unit cell
Υ	eV	Hopping energy between next nearest neighbors
$\hbar$	J/s	Reduced Planck constant
μ	$cm^{-2}V^{-1}s^{-1}$	Mobility
μ_n	$cm^{-2}V^{-1}s^{-1}$	Electron mobility
μ_p	$cm^{-2}V^{-1}s^{-1}$	Hole mobility
Ω	s^{-1}	Phonon frequency
Ψ	dimensionless	Wave function of the graphene sheet
ϵ_o	$As^2V^{-1}m^{-1}$	Dielectric constant
ϵ_{ox}	dimensionless	Relative dielectric constant of oxide layer
A	cm^{-2}	Area
$\vec{a_1}$	a_0	Vector of the unit cell
$\vec{a_2}$	a_0	Vector of the unit cell
c	$cm\ s^{-1}$	Speed of light
C_{gs}	μFcm^{-2}	Gate-source capacitance
$C_{gs\text{-}top}$	μFcm^{-2}	Gate-source capacitance due to top-gate voltage
$C_{gs\text{-}back}$	μFcm^{-2}	Gate-source capacitance due to back-gate voltage
C_{gd}	μFcm^{-2}	Gate-drain capacitance
$C_{gd\text{-}top}$	μFcm^{-2}	Gate-drain capacitance due to constant value of top-gate voltage
$C_{gd\text{-}back}$	μFcm^{-2}	Gate-drain capacitance due to constant value of back-gate voltage
C_{ox}	μFcm^{-2}	Oxide capacitance
$C_{ox\text{-}top}$	μFcm^{-2}	Top-gate oxide capacitance

$C_{ox\text{-}back}$	μFcm^{-2}	Back-gate oxide capacitance
C_g	μFcm^{-2}	Total gate capacitance
C_q	μFcm^{-2}	Quantum capacitance
$C_{q,min}$	μFcm^{-2}	Minimum value of the quantum capacitance
$C_{q,max}$	μFcm^{-2}	Maximum value of the quantum capacitance
D	$1/eV$	Density of states
Δx	cm	Step width
E	eV	Energy eigenvalue
E_F	eV	Fermi energy
E_{F^-}	eV	Quasi Fermi energy of left moving charge carriers
E_{F^+}	eV	Quasi Fermi energy of right moving charge carriers
E_C	eV	Conduction band minimum
E_V	eV	Valence band maximum
$E_{C,V}$	eV	Energy of the Dirac point
E_x	Vcm^{-1}	Electric field
E_{sat}	Vcm^{-1}	Saturation value of electric field
f_T	Hz	Cut-off frequency
g	dimensionless	Degeneracy factor
g_m	S	Transconductance
$g_{m\text{-}top}$	S	Transconductance due to top-gate voltage
$g_{m\text{-}back}$	S	Transconductance due to back-gate voltage
g_{ds}	S	Drain conductance
$g_{ds\text{-}top}$	S	Drain conductance due to constant of top-gate voltage
$g_{ds\text{-}back}$	S	Drain conductance due to constant of back-gate voltage
G	dimensionless	Intrinsic gain
G_{top}	dimensionless	Intrinsic top-gate gain
G_{back}	dimensionless	Intrinsic back-gate gain
I_d	A	Drain current
I_{sat}	A	Saturation current
$\vec{k}$	cm^{-1}	Wave vector measured from the K-point
$\vec{K}$	cm^{-1}	Wave vector measured from the F-point
k_B	J/K	Boltzmann constant

L	cm	Total channel length
n	cm^{-2}	Electron density per unit area
n_i	cm^{-2}	Intrinsic charge carrier density
N	dimensionless	Number of electrons in the device
N_p	dimensionless	Number of discretization points
n_{imp}	cm^{-2}	Impurity concentration
n_g	cm^{-2}	Carrier concentrations caused by the gate potential
n^*	cm^{-2}	Carrier concentrations caused by the charged impurities
p	cm^{-2}	Hole density per unit area
P	dimensionless	Number of electrons in the device
ρ_{sh}	cm^{-2}	Sheet charge density
$\rho_{sh,0}$	cm^{-2}	Residual sheet charge density
ρ_{real}	cm^{-2}	Absolute value of the ideal charge carrier density
q	As	Elementary charge
Q_{ch}	As	Channel charge
Q_{sh}	As	Net charge per unit area
$\vec{r}$	cm	Real space vector
$\vec{R}$	cm	Discrete lattice vector
s	dimensionless	+1 for the conduction band and −1 for the valence band
T	K	Kelvin temperature
t_{ox}	nm	Oxide layer thickness
t_{ox-top}	nm	Top-gate oxide layer thickness
$t_{ox-back}$	nm	Back-gate oxide layer thickness
v_F	cms^{-1}	Fermi velocity of the Dirac electron
V_{ch}	V	Channel potential
v_{drift}	cms^{-1}	Drift velocity
V_{ds}	V	Drain-source voltage
$V_{ds-kink}$	V	Drain-source voltage
V_g	V	Gate voltage
V_{gs-top}	V	Top-gate voltage

$V_{gs\text{-}top\text{-}ext}$	V	External top-gate voltage
$V_{gs\text{-}top\text{-}int}$	V	Internal top-gate voltage
$V_{gs\text{-}back}$	V	Back-gate voltage
$V_{gs\text{-}back\text{-}ext}$	V	External back-gate voltage
$V_{gs\text{-}back\text{-}int}$	V	Internal back-gate voltage
$V_{gs\text{-}top,0}$	V	Top gate-source voltage offset
$V_{gs\text{-}back,0}$	V	Back gate-source voltage offset
V_{ds}	V	Drain-source voltage
$V_{ds\text{-}ext}$	V	External drain-source voltage
$V_{ds\text{-}int}$	V	Internal drain-source voltage
$V(x)$	eV	Local channel potential
v_{sat}	V	Saturation velocity
U_{charge}	eV	Charging energy
R_s	Ω	Source resistance
R_d	Ω	Drain resistance
W	cm	Channel width
E	eV	energy eigenvalue
v_F	ms^{-1}	Fermi velocity
$D(E)$	/eV	Density of states (DOS)
a	m	Lattice constant
t_0	eV	$\hbar^2/2m^*a^2$
m^*	kg	Effective mass
L	m	Channel length
k	/m	wavector
U	eV	Self consistent potential
μ	eV	Electrochemical potential

f(E)	dimensionless	Fermi function
n(E)	/ eV	Electron density per unit energy
A(E)	/ eV	Spectral function
$G^n(E)$	/ eV	Correlation function
G(E)	/ eV	Retarded Green's function
T(E)	dimensionless	Transmission probability
$\gamma, \Gamma(E)$	eV	Broadening
$\sum(E)$	eV	Self energy (retarded)
$\sum^{in}(E)$	eV	In scattering

CHAPTER I

Introduction

1.1 Background

Graphene is a single layer of sp^2-bonded carbon atoms, that are packed in a honeycomb lattice. It wasn't until the year 2004 that Andre Geim and Konstantin Novoselov managed to produce graphene flakes with a technique called mechanical exfoliation. Geim and Novoselov were awarded the Nobel Prize in Physics in 2010 for their discovery of graphene. It is, therefore, easy to claim that 2010 has been the year of graphene [1].

Many theoretical and experimental works have been involved in investigating mechanical, electrical, and chemical properties of graphene. This one-atom-thick fabric of carbon uniquely combines many supreme properties that have been exceeded those obtained in any other material, with some reaching theoretically predicted limits: room-temperature electron mobility of 2.5×10^5 $cm^2V^{-1}s^{-1}$, high saturation velocity [2]-[4], very high thermal conductivity (above 3,000 WmK^{-1}), ability to sustain extremely high densities of electric current (a million time than copper) [5] and ballistic transport of charge carriers. The combination of these properties suggest that graphene could replace other materials in applications [6-14], including high speed and high frequency electronics, optoelectronic devices, touch screens, light emitting diodes, solar cells, sensors, individual gas molecules detectors, the applications where high sensitivity to electric charge, magnetic field and mechanical strength are required, and electrode material for capacitors in rechargeable batteries.

In addition, all the extreme properties are combined in one material means that glaphene could also enable several disruptive technologies. The combination of transparency, conductivity and elasticity will find use in flexible electronics, whereas transparency, impermeability and conductivity will find application in transparent protective coatings and barrier films; and the list of such combinations is continuously growing. A schematic of the high quality high quality large domain graphene by advanced synthesis method along with the current and future applications is shown in Figure 1.1.

Due to its high carrier mobility and ultrathin body, graphene has attracted tremendous attention as a channel material for future high speed nano-electronic devices. It is very interesting that, unlike other semiconduotors, graphene does not require impurity doping to conduct electricity. Graphene displays a phenomenon that is often called self-doping which refers to the electric field effect in graphene. It allows the charge carrier type and concentration to be controlled with an outside electric field, or rather gate voltage. In graphene, the charge carriers in the two dimensional channel can change from electrons to holes with the application of an electrostatic gate, with a minimum density point (or Dirac point characterizing the transition. The graphene band structure allows the conduction to shift from electrons to holes by changing the Fermi level. As explained above, Graphene is unique as a channel material for high speed field effect transistors.
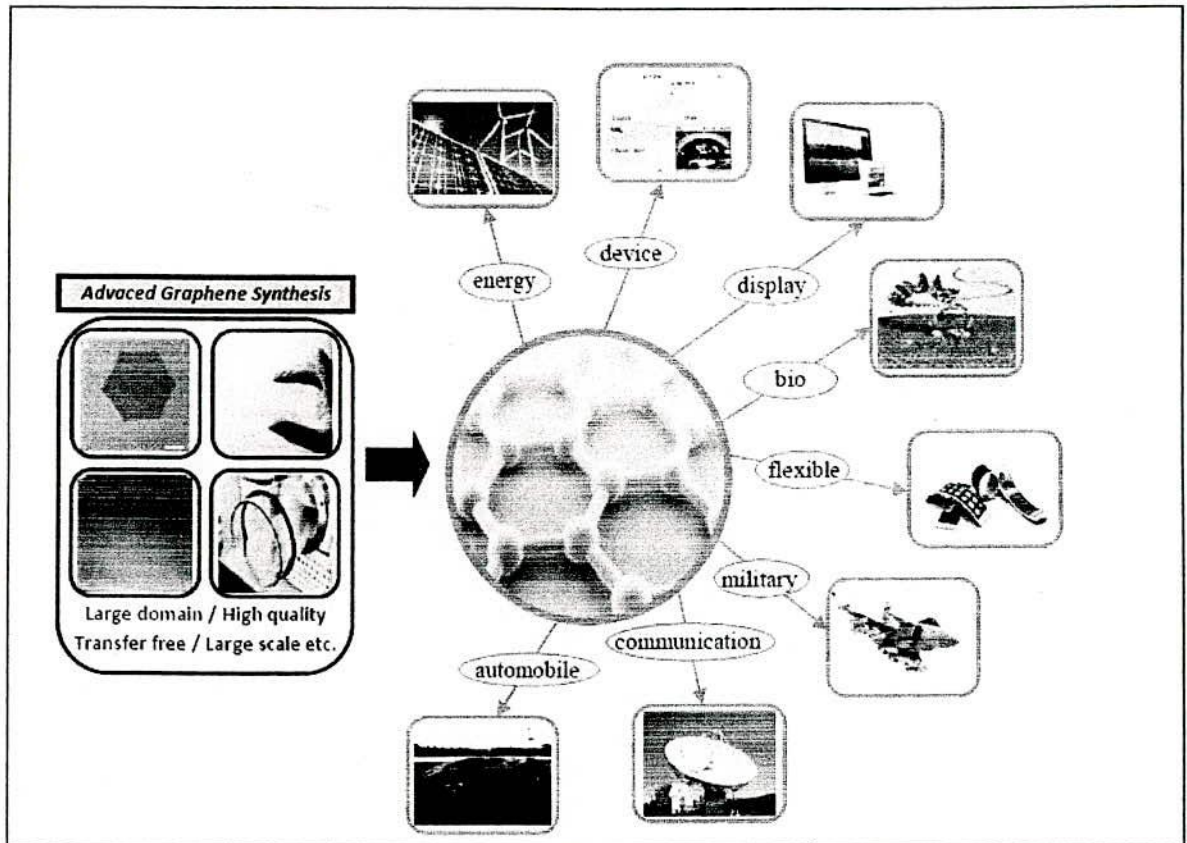
Figure 1.1: A schematic showing the high quality large domain graphene by advanced synthesis method along with the current and future applications.

1.2 Motivation

In an era when electronics components are becoming progressively smaller, saturation of conventional silicon technology and the limits to Moore's Law are frequently considered, the isolation of a single graphene layer represents a major technological achievement. Graphene is attractive for high speed field effect transistors and nanoelectronic applications due to its excellent electric properties. So, Graphene is very much promising material and considered as the best replacement of silicon for future generation transistor.

As the graphene is predicted to be potential candidate for electronic logic and RF applications, research is going on designing and fabrication of graphene FETs. However, the progress in designing and fabricating of graphene FETs is at initial stage. In order to fabricate high performance graphene FETs, understanding of detailed device modeling and performance evaluations is urgently required. There have been few works mostly on

Large area graphene field effect transistors (GFETs), but they are not sufficient for clear understanding of device physics and modeling. In addition, the works on ballistic GFET is very limited although GFET is promising for nanodevices. So, we have strongly motivated to work both on large area and ballistic graphene MOSFETs.

The aim of this thesis is to analyze the performance of a graphene MOSFETin large area and ballistic limit. The performance of a dual-gated large area graphene MOSFET is analyzed using analytical approach. The quantum transport simulation based on the NEGF formalism is used to analyze the performance of a top-gated graphene MOSFET in ballistic limit. The NEGF formalism is self-consistently coupled to the 1D Poisson equation. The Poisson equation is solved in 1D coordinate using the finite difference method (FDM).

1.3 Outline of Thesis

This dissertation is focused on study of graphene MOSFETs in aspects of large area and ballistic limit. The study has tried to gain insight into the potential of graphene MOSFETs for various applications by focusing on various figures of merit as applicable to different applications.

In chapter 2, Fundamentals of graphene MOSFET is reviewed.

Chapter 3 starts with the simulation approach including device model, analytical solution and bench marking of numerical solution of NEGF transport equation self consistently with Poisson equation.

Chapter 4 shows Performance of Graphene MOSFET in large area. The C-V characteristics is shown. Impurity Concentration Dependency of quantum capacitance is thoroughly investigated. The Current Voltage (I-V) Characteristics of large area graphene MOSFET and Channel Potential profile as well as sheet charge density profile is evaluated here.The velocity-field relationship is also illustrated.

In the chapter 5, a top gated graphene MOSFET is modeled in ballistic limit and corresponding I-V characteristics and transconductance profile is shown.

Finally, chapter 6 provides a summary of the most relevant results, combined with an outlook on possible future research directions.

CHAPTER II

Fundamental of Graphene

2.1 Invention of Graphene

Graphene is a fascinating material with many potential applications that stem from its unusual properties. The name graphene is sometimes misleadingly used with multiple layers, even though the variation in properties is quiet significant when going from one layer to several. It should be noted that multilayer graphene can have ten to ten layers, and still be called graphene. It was thought not to be stable in its free form until it was isolated in 2004 by researchers at The University of Manchester. The name "Graphene" was first mentioned in 1987 by S. Mouras and co-workers to describe the graphite layers that had various compounds inserted between them forming the so-called Graphite Intercalation Compounds or GIC's. Graphene was discovered at Manchester University by Russian-born scientists Andre Geim and Kostya Novoselov in 2004.

(a)

(b)
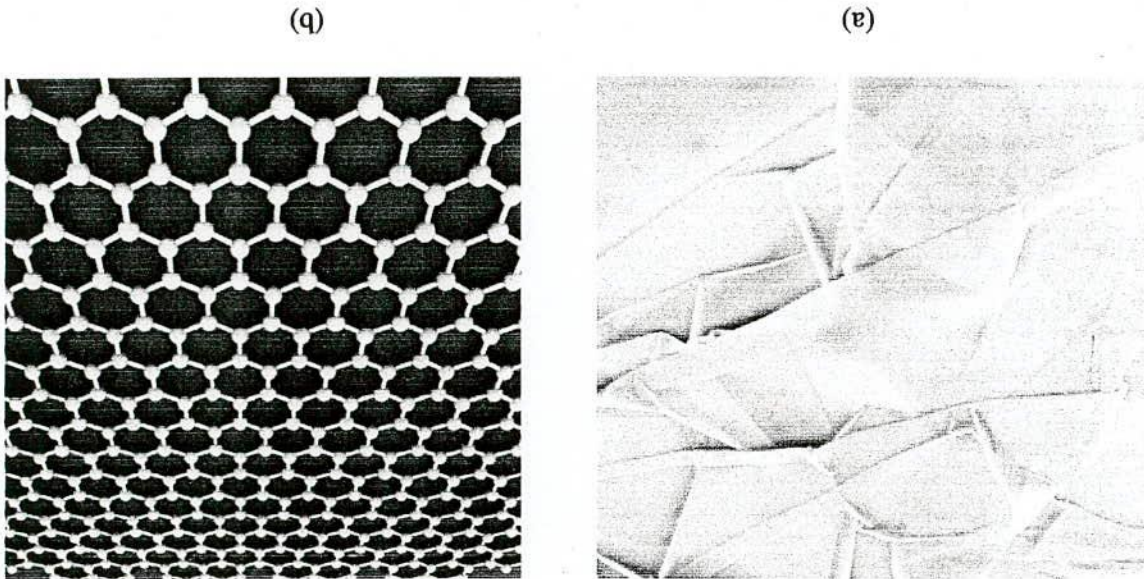
Figure 2.1: (a) Graphene is an atomic-scale honeycomb lattice made of carbon atoms. (b) SEM micrograph of a strongly crumpled graphene sheet on a Si wafer. (Online)

They won a Nobel Prize in 2010 for their discovery, which involved a roll of Scotch tape and some graphite. One forecast predicts the graphene industry will be commercially increased by 2022. That paper provided the inspiration for many groups around the world to redouble their efforts to study the properties of this material. Indeed, many groups sent students and post doctors to Manchester to learn how to make the material and much

fevered work was done to explore the unusual electronic properties of Graphene (online information). There may arise a question such as: Why is graphene such an exciting material? Firstly, graphene is great conductor; electrons are able to flow through graphene more easily than through even copper. The electrons travel through the graphene sheet as if they carry no mass, as fast as just one hundredth that of the speed of light. Secondly, the ways electrons behave in graphene make it very useful to study some fundamental physical properties. Graphene's near perfect crystal lattice mean it is a very clean system in which to experiment. Graphene is a one atom thick sheet made of carbon atoms, arranged in a honeycomb (hexagonal) lattice. Its height was measured to be just 0.33 nm, almost one million times thinner than a human hair!Graphene is the ultimate 2-dimensional carbon molecule. Graphite, the well-known 3-dimensional carbon allotrope found in our pencils, is nothing more than a stack of several graphene planes.Graphene shares its structure with two other materials which are exciting today's scientists: carbon nanotubes and fullerenes (also called bucky-balls), seen as a 1-dimension and 0-dimension rolled pieces of graphene, respectively.In 2004 Observation of graphene's ambipolar field effect by Andre Geim and Kostya Novoselov. In 2008 Measurements of extremely high carrier mobility of graphene was done by Bolotin also. New graphene related discoveries are in nanotechnology news almost every other day. Graphene is used in logical operations as well as radio-frequency applications.

2.2 Electronic Properties of Graphene

2.2.1 Electronic Band Structure

The electronic band structure of any material is responsible for its whole electronic behavior. Therefore it is important to understand where the band structure comes from and what assumptions were made. In this chapter, we will use the tight binding approach to calculate these energy bands. Graphene has a honeycomb (hexagonal) structure of sp^2-bonded atoms. The electronic band structure of graphene can be solved with tight binding approximation (TBA) or the similar linear-combination of atomic orbitals (LCAO), which is more commonly used in chemistry. The honeycomb lattice has 2 atoms per unit cell; hence the π bands of graphene have 2×2 Hamiltonian. The diagonal elements of the Hamiltonian describe the nearest neighbor interactions, while the off-diagonal elements describe the three nearest neighbor interactions in different sub lattices. The derivation of the electronic band structure is omitted here, but a detailed derivation in [16].

To calculate the electronic band structure, we have to consider the real space lattice. Graphene consists of sp^2-hybridized carbon atoms which are all situated in one plane and arranged in a honey comb lattice (Fig. 2.2(a)). Therefore, every carbon atom has three nearest neighbors and six next nearest neighbors. Each carbon atom possesses four valance electrons. Three of these electrons form tight σ bonds with the three neighbors atoms and do not contribute to the conductivity of graphene. The fourth electron is unbounded and considered to be in the $2p_z$ state. It has a node in the lattice plane and a symmetry axis perpendicular to it. The wave functions of all unbounded electrons overlap with those of neighbors, which is the reason for the conductivity of Graphene. First we define the unit cell of the graphene lattice (green dashed line in Fig. 2.2(a)). It has the

shape of the parallelogram and contains two different carbon atoms labeled I and II. The two vectors of the unit cell are labeled as $\vec{a_1}$ and $\vec{a_2}$. Since the crystal has a periodic structure one can conclude that probability to find an electron at the position $\vec{r}$ is equal to the probability to find an electron at the position $\vec{r}+\vec{R}$.

$$|\psi(\vec{r})|^2 = |\psi(\vec{r} + \vec{R})|^2 \qquad (2.1)$$

Where $\vec{R}$ is the discrete lattice vector and it can be expressed as a linear combination of the unit vectors?

a)   b)
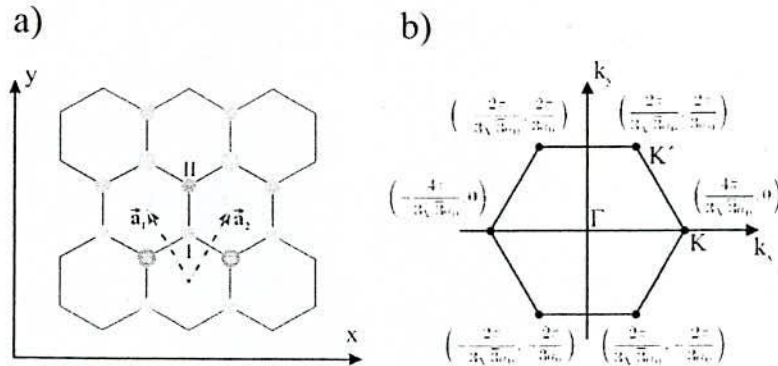
Figure 2.2: (a) The unit cell of the graphene real-space lattice is colored in green. It consists of two atoms labeled I and II. Atom I has three nearest neighbors colored in darker blue and 6 next nearest neighbors colored in light blue. Atom II has also three nearest neighbors colored in yellow and six next nearest neighbors colored in pink. The unit vectors of the lattice are labeled $\vec{a}_1$ and $\vec{a}_2$ (b) Displayed is the first Brillouin zone with the position of each K-point.

The band displayed in blue or orange in Fig. 2.3(a) is the conduction band or valance band, respectively. At 0 Kelvin the valance band is completely filled and the conduction band is empty. Therefore we might expect graphene to be an insulator or semiconductor, but the conduction band touches the valence band at the K-point of the Brillouin zone (Fig. 2.3(b)). Therefore the energy band gap of graphene is zero and $E_C = E_V = E_{C,V}$. Since the density of states at the intersection of the two bands is also zero graphene is a semi-metal. This osculation point if often referred to as the Dirac point. The background of this nomenclature is that the Hamiltonian of graphene around the K-point can also be written as the Dirac Hamiltonian.

a)   b)
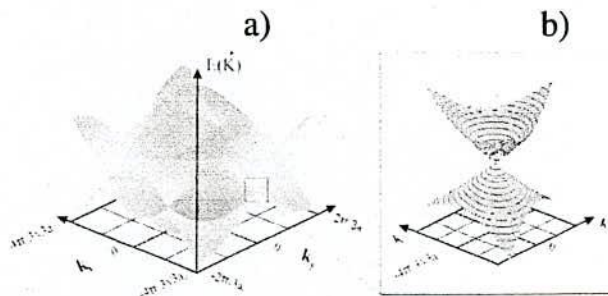
Figure 2.3: (a) The band structure of graphene is displayed. The valance band is colored in orange and the conduction band is colored in blue. (b) A magnified section around the K-point is shown.

We knew that,
$$E(\vec{K}) = \alpha \pm \beta \sqrt{3 + \omega(\vec{K})} + \Upsilon(\vec{K}) \qquad (2.2)$$

Here, $\vec{K}$ is the wave vector, E is the energy eigenvalue, α is the self-energy, β is the hopping energy between nearest neighbors and Υ is the hopping energy between next nearest neighbors. We can simplify eq. (2.2) by the Taylor series expansion:

$$E(\vec{K}) \approx \alpha + \frac{3}{2}a_0\beta|\vec{k}| + 3\gamma \qquad (2.3)$$

The wave vector $\vec{k}$ is measured from the K-point as point of origin, whereas $\vec{K}$ has its point of origin in the r-point. Therefore an electron with $|\vec{k}| = 0$ is situated at the K-point of the Brillouin zone or in other words at the Dirac point. Since only the absolute value of $\vec{k}$ is regarded, we will write $\vec{k}$ instead of $|\vec{k}|$. If we set $\alpha + 3\gamma = E_{C,V}$, we obtain:

$$E(k) - E_{C,V} \approx \pm \hbar \left(\frac{3a_0\beta}{2\hbar}\right)k \qquad (2.4)$$

Where, $v_F = \left(\frac{3a_0\beta}{2\hbar}\right)$ is the Fermi velocity. With $\beta = -3\ eV$, v_F becomes: $v_F = 970811$ m/s which is close to the value of $v_F = 10^6$ m/s which is usually found in papers and used in the following. Finally eq. (2.2) can be written as:

$$E(\vec{K}) - E_{C,V} = E(k) - E_{C,V} = s\hbar v_F k \qquad (2.5)$$

Where $s = +1$ in the conduction band and $s = -1$ in the valence band and $\hbar$ is the reduced Plank constant. Since the energy dispersion is linear around the K-point, one can see the energy band in the relativistic limit of the famous Einstein equation: $E = \sqrt{m^2c^4 + p^2c^2}$, where m is the mass, c the speed of light and p the impulse. If we set m to zero and c to v_F we recover eq. (2.5). Therefore charge carriers in this linear part of the band structure are often referred to as mass-less particles with an effective speed of light of v_F. The energy dispersion is linear around the K-point; therefore the velocity of an electron in the ballistic limit is independent of its energy E:

$$v = \frac{1}{\hbar}\frac{\partial E}{\partial k} = sv_F \qquad (2.6)$$

Graphene is a 2D material, but distinctions can be made between bi-layer graphene and few-layer graphene (FLG) [17]. Bilayer graphene has two layers, but the electronic band structure is already quite different from single layer graphene. Band gaps of some hundreds of milli electron volts have been achieved with bilayer graphene by applying a perpendicular electric field to the bilayer [18]. The gap in Bernal stacked bilayer graphene arises from the forming of pseudospin between the layers, thus making it possible to electrically induce a band gap [19]. There are still many properties of graphene that have not been thoroughly investigated. Even the existence of a band gap in large area graphene is controversial. In addition to band gap opening in bilayer graphene by applying an

electric field, it is possible to create band gap by quantum confinement, *i.e.* by fabricating graphene nanoribbons [17]. Band engineering of graphene is essential if graphene is ever to compete with silicon CMOS technology [19]. The energy gap is important for logic gate purposes to keep the power consumption at minimum *i.e.* going to a non-conductive state. The band-structure of graphene differs from the band-structures of semiconductors in that the energy dispersion around the band edges is linear instead of quadratic [20]. The mobility of charge carriers is limited by defects in the supporting material or defects in graphene. The previous claim is backed up by the much higher mobilities achieved with suspended graphene sheets. Electronic transport that is limited by scattering is called ballistic transport. Ballistic transport is possible in very pure and defect free graphene. Naturally, obtaining clean and defect free graphene is difficult and is often not achieved. The linearity of band dispersion in graphene means that the velocity of electrons is independent of energy or momentum. Furthermore, the velocity of electrons in graphene is at maximum the Fermi velocity, which is 1/300 of the speed of light. Another intriguing property is that backscattering through phonons or charged impurities is forbidden and the mean free path is in the range of hundreds of nanometers. The electrical properties of graphene have been studied extensively, but much is still un-known about the mechanical and thermal properties [21]. Mechanical and thermal properties of graphene are similar to those of carbon nanotubes. Measurements show that the breaking strength of graphene is around *40 N/m*, and thermal conductivity in the range of *5000 W/mK*, and yet the thermodynamic properties of graphene are largely unknown [21]. The chemistry of graphene is in early phases, but shows much promise. Graphene can absorb and desorb different atoms and molecules, such as *K* and *OH*. Adsorbents can affect the electronic properties of graphene. There is even the possibility of localized doping. In addition, the stability of graphene under various circumstances has not received much attention.

2.2.2 Density of States (DOS)

For the calculations of electronic properties not only the electronic band structure, but also the density of states (*DOS*) plays an important role. This quantity describes how many states per unit energy are available for occupation. It can be calculated in general using the following expression:

$$D^{2D} = g \frac{A}{(2\pi)^2} \int_{BZ}^{\infty} dk\, 2\pi k\, \delta(E - E(k)) \qquad (2.7)$$

Where g is the degeneracy factor, A the area, k the wave vector, E the energy and δ the Delta function. The integral of the Delta function is defined as $\int_{-\infty}^{+\infty} \delta(x)dx = 1$, *i.e.* every time the argument in the Delta function becomes zero the integral over the Delta function becomes one. Therefore, while integrating over the area in k-space in eq. (2.7), the Delta function simply counts the number of all the states where $E = E(k)$. In a periodic crystal each state can be occupied by an electron with spin up and with spin down which is expressed by a degeneracy factor of two. Furthermore the graphene unit cell contains two atoms (Fig. 2.1 (a)). The result is that each Brillouin zone contains two equivalent K-points, which gives an additional degeneracy factor of two. Since only electrons around the Fermi level are responsible for the electronic behavior it is sufficient to calculate the

DOS in the vicinity of the Dirac point. Therefore we can use eq. (2.7) to describe the *E (k)* behavior such as:

$$D^{2D}_{graphene} = \frac{2\pi}{A} \int_{BZ}^{\infty} dk k \delta(E - E_{C,V} - s\hbar v_F k) \tag{2.8}$$

This results in a density of states (*DOS*) as described [27]

$$D^{2D}_{graphene} = \frac{2A}{\pi} \frac{k}{\hbar v_f} \Big|_{k = \frac{E - E_{c,v}}{\hbar v_f}} \tag{2.9}$$

$$D^{2D}_{graphene} = \frac{2A}{\pi} \frac{|E - E_{c,v}|}{(\hbar v_f)^2} \tag{2.10}$$

The density of states for electrons and holes is always positive and increases linearly with energy. At the intersection of the valence and conduction band, *i.e.E* = *E_{C,V}* the *DOS* is zero. This behavior is different from two dimensional electron gases where the effective mass approximation can be applied. There the *DOS* is a Heaviside function and is not increasing linearly with energy.

2.2.3 Mobility of Graphene

The most frequently stated advantage of graphene is its high carrier mobility at room temperature.Mobilitiesof10,000-15,000cm^{2}V^{-1}s^{-1} are routinely measured for exfoliated graphene on *SiO*$_2$covered silicon wafers and upper limits of between40,000and70,000cm^{2}V^{-1}s^{-1} have been suggested. Moreover, in the absence of charged impurities and ripples, mobilities of 200,000cm^{2}V^{-1}s^{-1} have been predicted and a mobilityof10^6 cm^{2}V^{-1}s^{-1} was recently reported for suspended graphene [22]−[26].Finally, for epitaxial graphene on silicon carbide, themobility depends on whether the graphene is grown on the silicon face or the carbon face of *SiC*. Although graphene grown on the carbon face has higher mobility(valuesof~5,000cm^{2}V^{-1}s^{-1} have been reported compared with~1,000cm^2 V^{-1}s^{-1} for graphene grown on the silicon face, it is easier to grow single-layer and bilayer graphene on the siliconface,which makes the silicon face of *SiC* more suited for electronic applications. In early graphene MOS structures, the mobility was affected by the use of a top-gate dielectric. However, there has demonstration of mobilities of around 23,000cm^{2}V^{-1}s^{-1} intop-gated graphene MOS channels and the observation of similar mobilities before and after top-gate formation show that high-mobility graphene. The high mobilities mentioned above related to large-area graphene, which is gapless.

As general trend for conventional semi-conductors is that the electron mobility decreases as the bandgap increases, and a similar trend has been predicted for carbon nanotubes(CNTs) and graphene nanoribbons. Therefore, although the high mobilities offered by graphene can increase the speed of devices, they come at the expense of making it difficult to switch devices off, thus removing one of the main advantages of the CMOS configuration—its low static power consumption.

2.2.4 High-Field Transport

In the days when FETs had gates several micrometers long, the mobility was the appropriate measure of the speed of carrier transport. Strictly speaking, however, the mobility describes carrier transport in low electric fields; the short gate lengths in modern FETs result in high fields in a sizeable portion of the channel, reducing the relevance of mobility to device performance. To illustrate this, let us consider a FET with a gate 100 nm long and a drain–source voltage of 1 V. If we assume a voltage drop of 0.3V across the series resistances, the average field in the channel is $70kVcm^{-1}$ [27]. At such high fields, the steady-state carrier velocity saturates, and this saturation velocity becomes an other important measure of carrier transport. For graphene and the nanotube, maximum carrier velocities of around $4\times10^7cms^{-1}$ are predicted, in comparison with 2×10^7 cm s^{-1} for *GaAs* and 10^7 cms^{-1} for silicon. Moreover, at high fields the velocity in graphene and the nanotube does not drop as drastically as in the III–V semiconductors [17]. Unfortunately, there is at present no experimental data available on high-field transport in graphene nano ribbons and in large-area graphene. However, other measurements suggest high-field carrier velocities of several 10^7cm s^{-1} in graphene [28]–[29]. Thus, regarding high-field transport, graphene and nanotubes seem to have a slight advantage over conventional semiconductors. Finally, it is worth noting that reported mobilities for graphene devices need to be interpreted carefully because there are several definitions for the MOSFET channel mobility and they are difficult to compare. Furthermore, the techniques used to measure mobility are only vaguely described in some papers.

2.3 Further Option of Graphene Devices

It has become clear that graphene devices based on the conventional MOSFET principle suffer from some fundamental problems. This has motivated researchers to explore new graphene device concepts, such as tunnel FETs and bilayer pseudo spin FETs. In a tunnelFET, the band-to-band tunneling across the source–channel junction can be controlled using the gate-source voltage. The big advantage of tunnel FETs is that their subthreshold swings are not limited to 60mV per decade, as in conventional MOSFETs, which should lead to steeper subthreshold characteristics ad better switch-off. In particular, the bilayer graphene tunnel FET is now consider ed to be a promising device for a number of reasons: narrow nanoribbons are not needed, the small bandgap opened by a vertical field applied across the two layers is sufficient to suppress band-to-band tunneling in the off-state and thus enables effective switch-off; and the possibility of sub-threshold swings below 60mVper decade should make high on–off ratios possible. Although graphene tunnel FETs and bilayer pseudo spin FETs are both still at an embryonic stage, they have already gained considerable attention in the electron-device community. It might also be possible to make interconnects from graphene, which would open the possibility of all-graphene integrated circuits in which both the active devices and the wiring were made of graphene. It has been shown that graphene inter connects compete well with   copper   interconnects; indeed, graphene can support current

densities greater than 10^8 Acm^{-2} (which is 100 times higher than those supported by copper)and has a thermal conductivity of around 30–50 Wcm^{-1}K^{-1}(which is 4 Wcm^{-1}K^{-1} for copper).

CHAPTER III

Simulation Approach

3.1 Introduction

In earlier, The simulation of graphene MOSFET has been studied using different approaches. In this thesis, simulation of performance of graphene MOSFET is done in large area and ballistic limit. Analytical approach is used to simulate device performance large area graphene MOSFET. On the other hand, the Non-Equilibrium Green's Function (NEGF) [30] is used to simulate device performance in ballistic limit. The detailed theoretical discussion and formulation is given in this section.

3.2 Modeling of large area Graphene MOSFET

This thesis is about the modeling of large-area graphene metal-oxide semiconductor field-effect transistors (Graphene MOSFETs). Therefore a short revision of the basic working principle and the common nomenclature for field-effect transistors (FETs) is given. In every FET an electric field is used to change the conductivity of the channel. This electric field is generated by applying a gate voltage to the gate terminal. It controls how many electrons can pass through the channel. There are two other terminals in all FETs which are essential. These are the source and the drain terminal. Their names refer also to their functions. If a positive drain-source voltage is applied to these terminals, electrons are injected from the source into the channel and collected by the drain. The resulting current is referred to as the drain current. The feature which distinguishes GFETs from other FETs is that the channel is made of graphene.
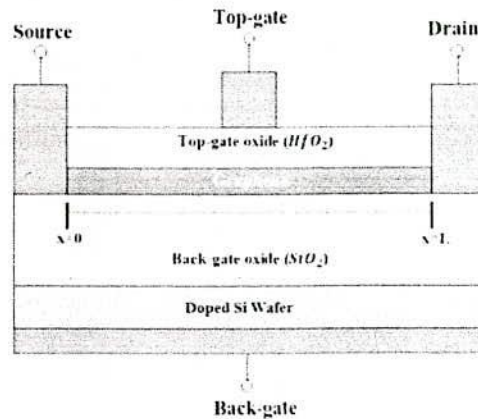
Figure 3.1: The cross section of the modeled graphene MOSFET with top- and back-gate.

A simple model of the GFET which is described in this thesis is shown in Fig. 3.1. Here the channel is made of large-area single-layer graphene, which has a zero band gap. It is located on a heavily doped oxidized silicon wafer. This acts as a second gate and is referred to as the back-gate. It is used to control whether the graphene is p- or n-conducting by applying a back-gate voltage. The source terminal is grounded and a drain-

source voltage can be applied to the drain terminal. Both contacts between these terminals and the channel are considered to be ohmic. The top-gate is separated from the graphene channel by an insulator and is used to control the charge carrier density and therefore the conductivity in the channel.

3.2.1 Charge carrier calculation

All considerations made in this chapter are for equilibrium conditions, *i.e.* no current is flowing. Therefore the drain-source voltage is *0V*. Furthermore the source terminal is considered to be grounded. The number of electrons in any material is calculated by performing the following integral [3]

$$N = \int_{E_c}^{\infty} dE D(E) f(E) \tag{3.1}$$

Where, $D(E)$ is the density of states and $f(E)$ is the Fermi function which is defined as $(e^{\frac{E-E_F}{k_B T}} + 1)^{-1}$. Inserting the density of states for graphene (eq. 2.10) and dividing by the area results in the charge carrier density n:

$$n = \frac{N}{A} = \int_{E_{c,v}}^{\infty} dE \frac{2}{\pi} \frac{E - E_{c,v}}{(\hbar v_F)^2} \frac{1}{e^{\frac{E-E_F}{k_B T}} + 1} \tag{3.2}$$

Where, E_F is the Fermi energy, q the element my charge, k_B the Boltzmann constant and T is the temperature. The same formalism can be applied for holes. Holes are defined as states in the valance band which are not occupied by electrons.

$$P = \int_{-\infty}^{E_v} dE D(E)(1 - f(E)) \tag{3.3}$$

Dividing by the area and inverting eq. (2.10) results in as mentioned below:

$$p = \frac{P}{A} = \int_{-\infty}^{E_{c,v}} dE \frac{2}{\pi} \frac{|E - E_{c,v}|}{(\hbar v_F)^2} \left(1 - \frac{1}{e^{\frac{E-E_F}{k_B T}} + 1} \right) \tag{3.4}$$

$$p = - \int_{E_{c,v}}^{-\infty} dE \frac{\pi}{2} \frac{|E - E_{c,v}|}{(\hbar v_F)^2} \left(\frac{1}{e^{-\frac{E-E_F}{k_B T}} + 1} \right) \tag{3.5}$$

We substitute E with $-E$, because we only want to deal with positive energies:

$$p = \int_{-E_{c,v}}^{\infty} dE \, \frac{\pi}{2} \frac{E + E_{C,V}}{(\hbar v_F)^2} \left(\frac{1}{e^{\frac{E+E_F}{k_B T}} + 1} \right)$$
(3.6)

For a gate voltage the Fermi energy of graphene is exactly between the conduction band and valence band (Fig. 3.2) as shown.
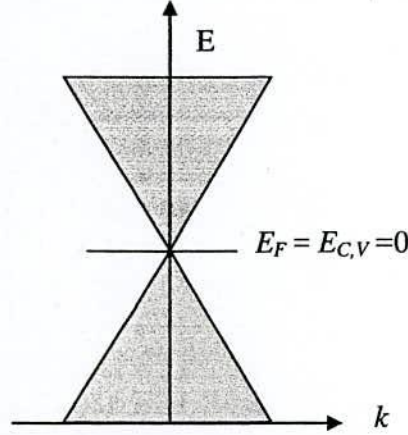
Figure 3.2: Fermi energy in undopedgraphene for zero gate and drain-source voltage.

This means that $E_F = E_{C,V} = 0$. Hence eq. (3.2) and eq. (3.6) simplify to as the following:

$$n = p = \frac{2}{\pi(\hbar v_F)^2} \int_0^{\infty} dE \left(\frac{E}{e^{\frac{E}{k_B T}} + 1} \right)$$
(3.7)

Since, this equation is equal for electrons and holes there is charge neutrality in the graphene layer. After substituting $u = \frac{E}{k_B T}$ we get. The integral can be solved analytically and gives $\frac{\pi^2}{12}$.

$$n = p = \frac{2}{\pi(\hbar v_F)^2} (k_B T)^2 \int_0^{\infty} du \left(\frac{u}{e^u + 1} \right)$$
(3.8)

$$n = p = n_i = \frac{\pi}{6} \left(\frac{k_B T}{\hbar v_F} \right)^2$$
(3.9)

We call this density the intrinsic charge carrier concentration. This means, if there are no impurities in graphene, n_i increases quadratically with the temperature and not exponentially due to the absence of a band gap and the linear dispersion relation [31].

If we apply a positive gate voltage to the gate terminal the energy bands are down-shifted by qV_{ch}, where V_{ch} is the channel potential (Fig. 3.3) and is defined as:

$$qV_{ch} = E_F - E_{C,V} \tag{3.10}$$

Thus a positive gate voltage results in a positive V_{ch}. Note that V_{ch} is normally not equal to V_g. The Fermi energy remains at zero ($E_F = 0$), since it is pinned to the drain and source Fermi level. Keep in mind that there is still no current flowing.
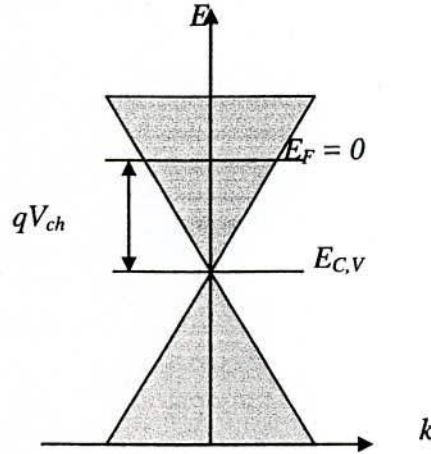
Figure 3.3: The energy bands are down-shifted with respect to the Fermi energy if a positive gate voltage is applied.

The carrier concentration can now be determined by solving the Fermi integral. Since $E_{C,V}$ is down-shifted by qV_{ch} with respect to E_F the lower integral boundary is $-qV_{ch}$.

$$n = \frac{2}{\pi(\hbar v_F)^2} \int_{-qV_{ch}}^{\infty} dE' \left(\frac{E' + qV_{ch}}{e^{\frac{E'}{k_B T}} + 1} \right) \tag{3.11}$$

Where E' is the energy. Now substitute $E = E' + qV_{ch}$ to change the integral boundaries.

$$n = \frac{2}{\pi(\hbar v_F)^2} \int_{0}^{\infty} dE \left(\frac{E}{e^{\frac{E - qV_{ch}}{k_B T}} + 1} \right) \tag{3.12}$$

If $qV_{ch} > 3k_B T$ the Fermi-Dirac distribution Eq. (3.12) reduces to as the following:

$$n = \frac{2}{\pi(\hbar v_F)^2} \int_{0}^{qV_{ch}} dE E \tag{3.13}$$

$$n = \frac{1}{\pi}\left(\frac{qV_{ch}}{\hbar v_F}\right)^2 \tag{3.14}$$

The electron concentration increases quadratically with V_{ch} for positive gate voltages.

Now we make the same considerations for holes while we are applying a positive gate voltage. The conduction band is again down-shifted by qV_{ch}. The lower integral boundary is $-E_{C,V}$ which becomes qV_{ch}. Therefore eq. (3.6) results in:

$$p = \frac{2}{\pi(\hbar v_F)^2}\int_{qV_{ch}}^{\infty} dE\left(\frac{E'-qV_{ch}}{e^{\frac{E'}{k_B T}}+1}\right) \tag{3.15}$$

Where, E' is again the energy, set $E = E' - qV_{ch}$ is made to change the integral boundaries.

$$p = \frac{2}{\pi(\hbar v_F)^2}\int_{0}^{\infty} dE\left(\frac{E}{e^{\frac{E+qV_{ch}}{k_B T}}+1}\right) \tag{3.16}$$

If $qV_{ch} > 3k_B T$ is then we can neglect the 1 in denominator, similar to the non-degenerate approximation in silicon. After performing this integral we obtain:

$$p = \int_{0}^{\infty} dE \frac{2}{\pi}\frac{E}{(\hbar v_F)^2} e^{-\frac{E+qV_{ch}}{k_B T}} \tag{3.17}$$

$$p = \frac{2}{\pi}\left(\frac{k_B T}{\hbar v_F}\right)^2 e^{-\frac{qV_{ch}}{k_B T}} \tag{3.18}$$

The hole concentration reduces exponentially with V_{ch} for positive gate voltages. Since the electron concentration increases only quadratically, there is no simple law of mass action as in the case of silicon.

$$n = \frac{2}{\pi}\left(\frac{k_B T}{\hbar v_F}\right)^2 e^{\frac{qV_{ch}}{k_B T}} \tag{3.19}$$

$$p = \frac{1}{\pi}\left(\frac{qV_{ch}}{\hbar v_F}\right)^2 \tag{3.20}$$

Note that, V_{ch} is also negative in this case. In some of the following calculations we are only interested in the sheet carrier density ρ_{sh} since the current is carried by both types of discharge carriers simultaneously. In this case it is convenient to neglect the minority charge carrier concentration and write:

$$\rho_{sh} = \frac{1}{\pi}\left(\frac{qV_{ch}}{\hbar v_F}\right)^2 \tag{3.21}$$

This equation becomes not only exact in the limit of zero Kelvin, but is also a rather good approximation for finite temperatures, since the minority charge carrier concentration is always decreasing exponentially. Sometimes it is useful to rewrite this expression by substitution qV_{ch} with $E_F - E_{C,V}$.

$$|E_F - E_{C,V}| = \hbar v_F \sqrt{\pi\rho_{sh}} \tag{3.22}$$

3.2.2 Quantum Capacitance

The concept of quantum capacitance was first introduced by S. Luryi in 1988 [32] for a two dimensional electron gas (*2DEG*) and will now be applied to graphene. The effect of the quantum capacitance is rather negligible in devices with a large density of states (*DOS*). Although the effect of quantum capacitance has not drawn attention in the past, since the devices were too large. By the time carbon nanotube transistors where intensively investigated, the quantum capacitance became again more important. Later on the concept was introduced first for graphene nanoribbons and afterwards also for large-area graphene. It will be shown that the quantum capacitance has a strong influence on the total gate capacitance and must therefore be included into the modeling.

The quantum capacitance has a non-zero minimum at the Dirac point and a linear increase on both sides of the minimum with relatively small slopes. The theoretical nature of C_q curve is not same as the experimental curve because charged impurities also influence the quantum capacitance. The long-standing puzzle about the interfacial capacitance in carbon-based electrodes has a quantum origin. The electron transport properties of graphene devices are very critical and these properties are still incomplete. One of the most important matters is the minimum in the conductivity at the Dirac point. This minimum is due to charged impurities that induce of electrons and holes in the graphene. To fully understand the transport properties it is important to such factors which are related to C_q.

    i)   The scattering of the carriers by the charged impurities.
    ii) The density of the carriers at and near the Dirac point.

Electron transport in graphene on the field-effect transistor (FET) configuration in which graphene sample is placed on SiO_2 substrate and connected to the source and drain electrodes. The graphene is used as the channel of the MOSFET.

The parallel plate capacitor with capacitance, $C = \frac{\epsilon_0 \epsilon_{ox}}{t_{ox}} \mu F cm^{-2}$. Where ϵ_{ox} and t_{ox} are the dielectric constant and the thickness of the substrate oxide layer which acts as the insulator

substrate. The oxide capacitance *i.e.* top gate capacitance or back gate capacitance does not strongly dependent on the gate potential *i.e.* top gate potential or back gate potential.

The quantum capacitance (C_q) depends on the net channel charge density which comes from the term two dimensional electron gas (*2DEG*). The overall net mobile sheet charge density Q_{sh} is simply the difference between the hole and electron sheet densities multiplied by the elementary charge. An exact derivation for C_q will now be given for large-area graphene. Since C_q is the first derivative of the net charge per unit area in the graphene sheet with respect to V_{ch}, we will first have a look at Q_{sh}. Generally it can be calculated by:

$$Q_{sh} = q\,(p\text{-}n) \tag{3.23}$$

Where n and p are the electron and hole concentration, q is the elementary charge. Since only the net charge is regarded, electrons have to be subtracted from holes. By inserting eq. (3.12) and eq. (3.16) this expression can be expanded to:

$$Q_{sh} = q\,\frac{2}{\pi(\hbar v_F)2}\int_0^\infty dE\;E\left(\frac{1}{e^{\frac{E+qV_{ch}}{k_B T}}+1} - \frac{1}{e^{\frac{E-qV_{ch}}{k_B T}}+1}\right) \tag{3.24}$$

The quantum capacitance is defined as the derivative of the net channel sheet charge density Q_{sh} with respect to V_{ch} [31]

$$C_q = -\frac{dQ_{sh}}{dV_{ch}} \tag{3.25}$$

The minus sign indicates that a more positive gate voltage results in a more positive channel voltage and thus leads to a more negative charge in the channel. The expression for quantum capacitance was derived based on a two dimensional electron gas (*2DEG*) model [33]. The exact equation for the quantum capacitance C_q as follows [31]

$$C_q = \frac{2q^2 k_B T}{\pi(\hbar v_F)2}\ln\left\{2\left(1 + \cosh\left(\frac{qV_{ch}}{k_B T}\right)\right)\right\} \tag{3.26}$$

Where, $v_F \approx c/300 = \frac{3\times10^8}{300} = 1\times10^6$ ms^{-1} = 1×10^8 cms^{-1} is the Fermi velocity of the Dirac electron and $V_{ch}=E_F/q$ is the potential of the graphene. Here, k_B is the Boltzmann constant, $\hbar$ is the reduced Plank's constant and T is the Kelvin temperature.

For $qV_{ch}>3K_B T \cong$ **75 meV** we can neglect the 1 in the logarithm and then equation (3.26) can be simplified to as the following [33]

$$C_q \approx \frac{2q^2}{\pi}\frac{q\,|V_{ch}|}{(\hbar v_F)2} \tag{3.27}$$

$$C_q = \frac{2\,q^2 q V_{ch}}{\pi(\hbar\,v_F)2} = \frac{2\,q^2}{\sqrt{\pi}\,\hbar\,v_F}\sqrt{n} \qquad (3.28)$$

Where $n = \frac{1}{\pi}\left(\frac{qV_{ch}}{\hbar\,v_F}\right)^2$ is the carrier concentration of the grapheme channel of a GFET.

3.2.3 Impurity Concentration Dependency of C_Q

The impurity concentration has a great effect on the quantum capacitance [33]. Several important features are worth noting to calculate the quantum capacitance C_q.

i) The quantum capacitance has a minimum value at the Dirac point ($C_{q,min}$).
ii) The minimum value of the quantum capacitance ($C_{q,min}$) is close to zero.
iii) The capacitance increases linearly with V_{ch} with a fixed slop ($\mu Fcm^{-2}V^{-1}$).
iv) The shape of the $C_q - V_{ch}$ curve is symmetric with respect to the Dirac point.

Several distinct discrepancies: the measured quantum capacitance minimum ($C_{q,min}$) is round and the measured minimum ($C_{q,min}$) is much greater than the predicted value of C_q. If the value of V_{ch} is zero then $\cosh(0) \cong 1$. So the minimum value of C_q is as follows:

$$C_{q,min} = \frac{2\,q^2 k_B\,T}{\pi(\hbar\,v_F)2}\,ln[2 + (1 + 1)] \qquad (3.29)$$

$$C_{q,min} = \frac{2\,q^2 k_B\,T}{\pi(\hbar\,v_F)2}\,ln[4] \qquad (3.30)$$

At room temperature $T = 298K$ the value of $C_{q,min}= 0.8358$ µFcm^{-2} and if $T = 300K$ then the value of $C_{q,min}= 0.8414$ µFcm^{-2} i.e. approximately $C_{q,min} \cong 0.8$ µFcm^{-2}. The theoretical model is based on the assumption of pure and perfect graphene. In reality, various impurities and defects exist in the oxide substrate. The recent theoretical and experimental results have shown that charged impurities have a key role in the transport properties of graphene near the Dirac point. It has been reported that charged impurities in substrates cause local potential fluctuations and electron or hole puddles in graphene. Additional carrier density n^* induced by the impurities. This additional carrier density should take into account by expressing the total carrier concentration as [31]:

$$n = |\,n_g\,| + |n^*| \qquad (3.31)$$

Where n_g and n^* are the carrier concentrations caused by the gate potential and the charged impurities respectively. Combining equation (3.28) and (3.31) we can calculate the quantum capacitance of graphene as a function of the graphene potential and the different impurity concentration of the oxide substrate which is used as the insulator of a GFET:

$$C_q = \frac{2\,q^2\,qV_{ch}}{\pi(\hbar\,v_F)2} = \frac{2\,q^2}{\sqrt{\pi}\,\hbar\,v_F}\sqrt{|n_g| + |n^*|} \tag{3.32}$$

Where $n_g = (\frac{qV_{ch}}{\sqrt{\pi}\hbar\,v_F})^2$ is the carrier concentration due to gate voltage and channel potential. Now we have to think about the residual charge concentration n^* as a function of charged impurity concentration n_{imp} for two different dielectric material HfO_2 ($\epsilon_{ox}= 16$) and SiO_2 ($\epsilon_{ox}=3.9$)[35]. Because we have used HfO_2 as the top gate dielectric material, so the impurity concentration has to be considered for this type of material also.

In our model we have used only single impurity density ($n^*=8\times10^{11}$ cm^{-2}) throughout the total model or characteristics of the GFET. The inclusion of the impurity contribution explains the experimental results well. First, at zero channel potential ($V_{ch} = 0$) the value of $n_g=0$ and the quantum capacitance is finite and determined by the effective or residual concentration n^* [35]. Secondly, the slopes of the linear regime on both sides of the capacitance minimum are reduced by the charged impurities. Thirdly, the capacitance minimum regime is round. As the value of residual concentration or carrier concentration caused by charged impurities n^* increases, the minimum region becomes increasingly round and the slopes decrease. There are some procedures to calculate the value of carrier concentration caused by charged impurities of the substrate layer [35].

To determine the peculiar interfacial capacitance of the carbon electrodes has a quantum origin. Finally, the quantum capacitance model is consistent with the recent observation of Dirac fermions or two dimensional electron and hole gases (2DEG, 2DHG) at the surface of graphite. A complete interfacial capacitance theory includes both the quantum contribution and impurities are yet to be developed. The importance of charged impurities (n^*) is for both mobility (μ) and quantum capacitance (C_q).

3.2.4 Self-Consistent Quantum Capacitance

The charge carrier density ρ_{sh} in the graphene channel is the absolute value of the net amount of mobile charge carriers Q_{sh} divided by the elementary charge q [33]

$$Q_{sh} = -\frac{1}{2}C_q V_{ch} \tag{3.33}$$

$$\rho_{sh} = -\frac{1}{2q}C_q|V_{ch}| \tag{3.34}$$

If we assume V_{ch} to be positive we would obtain a negative charge which corresponds to an accumulation of electrons. Note that eq. (3.33) is the Poisson equation in one dimension, what is much easier to solve than the usual second order differential equation. One should mention that in this simple equation the minority charge carriers are neglected, this is a very good approximation due to their exponential decrease with V_{ch}. It is also worth to mention that in contrary to a parallel plate capacitor where $Q = C.V$, we get an

additional factor of $\frac{1}{2}$ for graphene. This can be explained by the fact, that C_q is a function of V_{ch} and cannot be pulled out of the integral, as in the case of a parallel plate capacitor.

In general it is more useful to calculate ρ_{sh}, in terms of V_g rather than in terms of V_{ch}. Therefore V_{ch} in eq. (3.33) has to be expressed by V_g. From the equivalent capacitive circuit in Fig. 4.1 we can write,

$$Q_{sh} = -\frac{1}{2} C_q V_{ch} = -C_{ox} V_{ox} \tag{3.35}$$

Now, we get for V_{ch} and the relation between V_{ch}, V_{ox} and V_g are mentioned below such as:

$$V_{ch} = V_{ox} \frac{C_{ox}}{\frac{1}{2}C_q} \tag{3.36}$$

$$V_{ox} = V_g - V_{ch} \tag{3.37}$$

By combining the eq. (3.36) and eq. (3.37) we can get the exact relation as the following:

$$V_{ch} = V_g \frac{C_{ox}}{\frac{1}{2}C_q + C_{ox}} \tag{3.38}$$

An easy and quite general way to solve eq. (3.38) numerically is to perform a self-consistent loop, i.e. the equations for C_q and V_{ch} have to be solved simultaneously. In the following the algorithm is briefly explained.

$$C_{q-old} = C_q \tag{3.39}$$

$$V_{ch} = V_{ch}(C_{q-old}) \tag{3.40}$$

$$C_q = C_q(V_{gs-top}, V_{gs-back} V_{ch}) \tag{3.41}$$

First an initial C_q must be guessed. Afterwards we assign C_q to C_{q-old} then C_q is calculated using eq. (3.32) and subsequently C_q is calculated using eq. (3.38). Then the new C_q is compared with C_{q-old}. If their difference is larger than a certain limit δ, the loop is started again. The loop terminates if $|C_{q-old} - C_q| < \delta$. The smaller δ is chosen the better is the approximation we get for C_q, but the more interactions are needed. Therefore a compromise between accuracy and computing time is necessary.

Now we substitute eq. (3.38) into eq. (3.33) and get as

$$Q_{sh} = -V_g \frac{\frac{1}{2}C_q C_{ox}}{\frac{1}{2}C_q + C_{ox}}$$ (3.42)

We can express this also in terms of charge carrier density

$$q\rho_{sh} = |V_g| \frac{\frac{1}{2}C_q C_{ox}}{\frac{1}{2}C_q + C_{ox}}$$ (3.43)

Thus the self-consistent quantum capacitance could be found. And the theory is consistent.

3.2.5 Equivalent Capacitive Circuit

If we add the back gate-oxide capacitance $C_{ox\text{-}back}$ to the series connection of C_q and $C_{ox\text{-}top}$, it should not make a difference which of the two capacitances belongs to the top-gate and which to the back-gate. If we set one of these capacitances to zero, we should end up with a series connection of the remaining oxide capacitance and the quantum capacitance. Since we also want to describe non-equilibrium conditions *i.e.* we allow carrier transport by applying a drain-source voltage V_{ds}, an additional parameter $V(x)$ is introduced. It takes the voltage drop inside the graphene channel, due to the current flow, into account. It is $V=0$ at $x = 0$ and V_{ds} at $x = L$. The new equivalent capacitive network is displayed in Fig. 3.4.
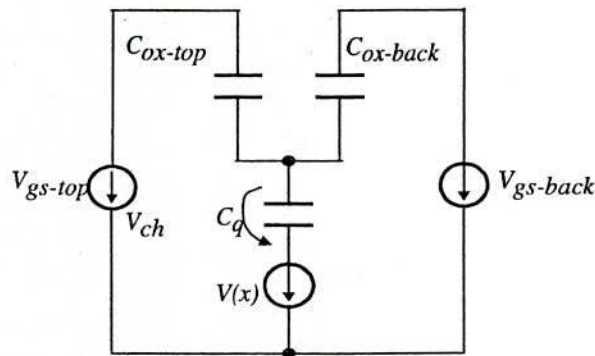
Figure 3.4: Equivalent capacitive circuit of a graphene MOSFET with both top-gate and back-gate. Here, $C_{ox\text{-}top}$, $C_{ox\text{-}back}$ are the top-gate and back-gate oxide capacitance respectively. The applied top-gate voltage is $V_{gs\text{-}top}$ and the applied back-gate voltage is $V_{gs\text{-}back}$. The potential drop due to the finite resistance in the channel is $V(x)$ and the difference between the Fermi energy and the conduction band minimum is V_{ch} [33]

Since we can calculate all components In the equivalent capacitive circuit, we are able to determine the charge in the graphene channel Q_{sh} in terms of $V_{gs\text{-}top}$ and $V_{gs\text{-}back}$. By applying Kirchhoff's laws to the equivalent circuit in Fig. 3.4 we end up three equations:

$$V_{gs\text{-}top} - V(x) = Q_{ox\text{-}top}/C_{ox\text{-}top} + Q_{sh}/\frac{1}{2}C_q \tag{3.44}$$

$$V_{gs\text{-}back} - V(x) = Q_{ox\text{-}back}/C_{ox\text{-}back} + Q_{sh}/\frac{1}{2}C_q \tag{3.45}$$

$$Q_{sh} = Q_{ox\text{-}top} + Q_{ox\text{-}back} \tag{3.46}$$

Now we have three independent equations with three unknowns Q_{sh} $Q_{ox\text{-}top}$, $Q_{ox\text{-}back}$. Therefore we can solve these equations and write an expression for $V_{ch} = Q_{sh}/\frac{1}{2}C_q$.

$$V_{ch} = (V_{gs\text{-}top} - V(x)) \frac{C_{ox\text{-}top}}{C_{ox\text{-}top} + C_{ox\text{-}back} + \frac{1}{2}C_q} + (V_{gs\text{-}back} - V(x)) \frac{C_{ox\text{-}back}}{C_{ox\text{-}top} + C_{ox\text{-}back} + \frac{1}{2}C_q} \tag{3.47}$$

If we set $C_{ox\text{-}back}$ and $V(x)$ to zero we would end up with eq. (3.38), because Fig. 3.2 is only a special case of Fig. 3.4.. The charge carrier density is calculated by using eq. (3.33) as:

$$-Q_{sh} = (V_{gs\text{-}top} - V(x)) \frac{\frac{1}{2}C_{ox\text{-}top}\,C_q}{C_{ox\text{-}top} + C_{ox\text{-}back} + \frac{1}{2}C_q} + (V_{gs\text{-}back} - V(x)) \frac{\frac{1}{2}C_{ox\text{-}back}\,C_q}{C_{ox\text{-}top} + C_{ox\text{-}back} + \frac{1}{2}C_q} \tag{3.48}$$

In terms of charge carrier density equation (3.48) modifies to as the following:

$$q\rho_{sh} = |-Q_{sh}| \tag{3.49}$$

The influence of this electrical potential can be modeled by the additional voltages $V_{gs\text{-}top,0}$ and $V_{gs\text{-}back,0}$. The voltage $V_{gs\text{-}top,0}$ is the voltage which needs to be applied to the top-gate in order to move the Fermi level E_F to $E_{C,V}$ and the voltage $V_{gs\text{-}back,0}$ is defined analogously.

$$q\rho_{sh} = \left| (V_{gs\text{-}top} - V(x) - V_{gs\text{-}top,0}) \frac{\frac{1}{2}C_{ox\text{-}top}\,C_q}{C_{ox\text{-}top} + C_{ox\text{-}back} + \frac{1}{2}C_q} + \right.$$
$$\left. (V_{gs\text{-}back} - V(x) - V_{gs\text{-}back,0}) \frac{\frac{1}{2}C_{ox\text{-}back}\,C_q}{C_{ox\text{-}top} + C_{ox\text{-}back} + \frac{1}{2}C_q} \right| \tag{3.50}$$

In real graphene there are defects and thermally induced charge carriers [33]. To determine the real charge carrier density we simply add this residual density ($\rho_{sh,0}$) to the ρ_{sh} asbelow:

$$\rho_{real} = \rho_{sh}(V_{gs\text{-}top}, V_{gs\text{-}back}, V_x) + \rho_{sh,0} \tag{3.51}$$

3.2.6 Channel Potential Calculation

The channel potential of dual gated, large area graphene MOSFETs can be calculated in different techniques. We have followed the model [36]. The main feature of this model is to feed a drain current into the device and applying the top-gate and back-gate voltages to calculate the resulting channel potential as well as drain source voltage [34]. Here, only the drift current is considered and the effect of the self-consistent quantum capacitance is taken into account using eq. (3.32) and eq. (3.47). First, the channel length is divided into several equidistant segments as shown in Fig. 3.5. The length of the small segment is $\Delta x = L/N$, where L is the channel length and N is the total number of small segments. Initially a drain current I_d is feed into this model and top-gate voltage $V_{gs\text{-}top}$, back-gate voltage $V_{gs\text{-}back}$ is applied and using the parameters in Table-III the channel potential is calculated. Since the current is negative the channel acts as a p-type MOSFET. To get the channel potential $V(x)$ which is dependent on the position of the channel length x from 0 to L, the parasitic source-drain resistances (i.e. R_s and R_d) are not considered for potential calculation.
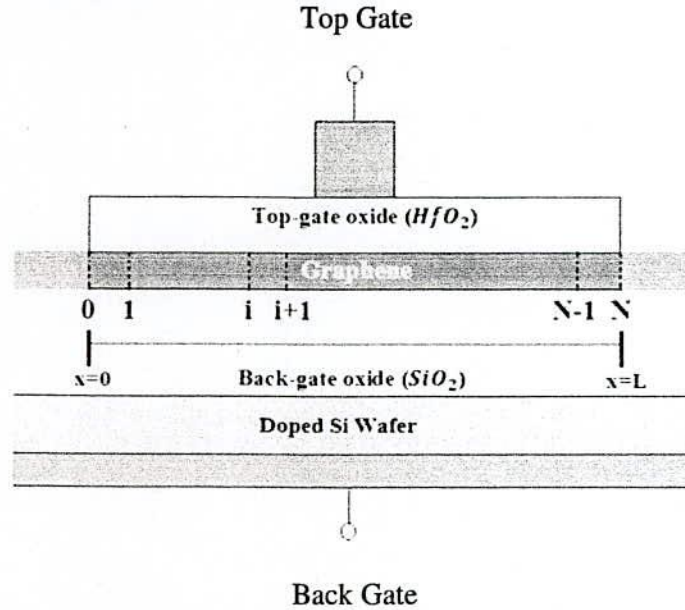

Figure 3.5: The cross section of the discretized Graphene channel.

At position $x=0$ the initial values $V(x)$, $\rho(x)$, $v(x)$, $E(x)$ are calculated. At $x=0$, the channel potential is $V(x=0)=V(i=0)=0$. The first step is to divide the GFET channel into equidistant pieces in space (Fig. 3.5). If the number of discretization is N, the length of one element is $\Delta x = L/N$. It is mentioned that $x = i \times \Delta x$, where $i = 0$ to N i.e. the number of the values of i is $N+1$. Using $V(x)=0$ the self-consistent quantum capacitance C_q ($i\Delta x = 0$) is calculated as mentioned in section 4.4. Then potential across the quantum capacitance V_{ch} ($i\Delta x = 0$) is calculated by using (3.47). The corresponding sheet charge density $\rho_{sh}(i\Delta x = 0)$, saturation velocity $v_{sat}(i\Delta x = 0)$ are calculated by using (5.1), (5.3) respectively. Due to the current continuity the

drift velocity $v(i \Delta x = 0)$, electric field $E(i \Delta x = 0)$ are calculated as the following equations [34].

$$\rho_{sh}(i\Delta x=0) = \left| -\frac{1}{2q} C_q(i\Delta x = 0) \, V_{ch}(i\Delta x = 0) \right| + \rho_{sh,0} \tag{3.52}$$

$$v(i\Delta x=0) = \frac{I_d}{qW\rho_{sh}(i\Delta x=0)} \tag{3.53}$$

$$v_{sat}(i\Delta x=0) = \frac{2\hbar\Omega}{\pi^2\hbar^2 v_F \rho_{sh}(i\Delta x=0)} \sqrt{\pi(\hbar v_F)^2 \rho_{sh}(i\Delta x = 0) - \left(\frac{\hbar\Omega}{2}\right)^2} \tag{3.54}$$

$$E(i\Delta x=0) = \frac{|v(i\Delta x=0)| \times v_{sat}(i\Delta x=0)}{\mu\sqrt{v_{sat}(i\Delta x=0)^2 - v(i\Delta x=0)^2}} \tag{3.56}$$

The channel potential in the next segment *i.e.* $i=i+1$ iscalculated by:

$$V[(i+1)\Delta x = \Delta x] = V(i\Delta x = 0) - E(i\Delta x = 0) \times \Delta x \tag{3.57}$$

This algorithm is repeated by calculating the sheet charge density at $x = (i+1) \times \Delta x$. Thus applying this procedure until $i=N$ and the total channel potential $V(N\Delta x)$ is calculated. If the drift velocity $v(i\Delta x)$ exceeds the saturation velocity $(2v_F/\pi)$ then the sheet charge density $\rho(i\Delta x)$ will be too small to guarantee current continuity. In this condition the drift velocity is set to maximum saturation velocity and sheet charge density is set to as follows [36].

$$v(i\Delta x) = v_{sat} = 2v_F/\pi \tag{3.58}$$

$$\rho(i\Delta x) = \frac{I_d}{qWv_{sat}} = \frac{\pi I_d}{2qWv_F} \tag{3.59}$$

When $v(x) = v_{sat}(x)$ the electric field E_{sat} would be infinitely large and E_{sat} is calculated by

$$E(i\Delta x) = a\frac{v(i\Delta x)}{\mu} = a\frac{2v_F}{\pi\mu} \tag{3.60}$$

Where a is an empirical factor such as *4* or *5* used only in the region of constant electric field at $v(x) = v_{sat}(x)$. By this procedure the channel potential of graphene MOSFET is calculated.

3.2.7 Saturation Characteristics

The saturation current is computed by the Landauer formula as derived by here briefly [34]

$$I_{sat} = \frac{2qW\Omega}{\pi^2\hbar v_F} \sqrt{\pi(\hbar v_F)^2 \rho_{sh} - \left(\frac{\hbar\Omega}{2}\right)^2} \tag{3.61}$$

And the corresponding saturation velocity is given by:

$$V_{sat} = \frac{2\hbar\Omega}{\pi^2\hbar^2 v_F \rho_{sh}} \sqrt{\pi(\hbar v_F)^2 \rho_{sh} - \left(\frac{\hbar\Omega}{2}\right)^2} \tag{3.62}$$

Therefore the saturation velocity (v_{sat}) depends on sheet charge density (ρ_{sh}) which is a specific feature of graphene and has to be considered in the calculations.

The saturation velocity is linked to the saturation current I_{sat} by:

$$I_{d,sat} = qW \frac{2v_F}{\pi} \rho_{sh} \tag{3.63}$$

The equation (5.11) we can get the relation between v_{sat} and v_F as:

$$v_{sat} = \frac{2v_F}{\pi} \tag{3.64}$$

The index 1 is only introduced to distinguish between saturation velocity above and the one which will be obtained in the next step. It is interesting to note that this saturation velocity corresponds to the average velocity of electrons moving in $+x$ direction, which is simultaneously the ballistic velocity. The saturation velocity is considered in our model [36].

3.2.8 DC Characteristics

There are some methods of simulating GFET characteristics into computer. In this section one method to model the output characteristics of graphene FETs is mentioned. Here, a different approach is developed. The main procedure of this model is to calculate the drain-source voltage (V_{ds}) for a given drain current (I_d). The current-voltage characteristics of the dual gated GFET are fully discussed by this model [34]. The drain-source current versus drain-source voltage ($I_{ds}-V_{ds}$) characteristics was found with different values of top-gate and back-gate voltages. On the other hand the drain current versus top-gate voltage ($I_{ds}-V_{gs-top}$) and the drain current versus back-gate voltage ($I_{ds}-V_{gs-back}$) with different drain-source voltages were also found. The drift velocity (v_{drift}) and electric field (E_x) were discussed by this method. The parasitic drain and source resistance are taken into account also. After all the saturation velocity and saturation current characteristics were also found. Finally, the maximum DC characteristics of GFET were calculated and discussed in this section.

The assumptions made in the previous model are mentioned below which are essential.

  i.   Only the drift current is considered and diffusion current is neglected.
  ii. The effect of the quantum capacitance on the charge carrier density is taken into account throughout the whole procedure of this model.
  iii. Only the majority charge carriers (electrons or holes) are included in this model and the minority charge carriers (holes or electrons) are neglected here.
  iv. A velocity-electric field characteristic with soft saturation is considered.

v.   The saturation velocity depends on the charge carrier density but can't exceed the value $\frac{2v_F}{\pi}$ ever.

vi.   The electric field in the region where $v = v_{sat}$ is set to be constant also.

vii.   The parasitic source and drain series resistance are taken into account.

The current-voltage characteristics are found by following both the section 4.4 and section 5.3 approximations. Here, I_d–V_{ds} characteristics of graphene MOSFETs are found by setting channel potential at source end with $I_d R_s$ at $x = 0$ [34].

$$V(x=0) = V(i=0) = I_d R_s \qquad (3.65)$$

By applying the procedure of Section 5.3 until $i = N$ and adding potential $I_d\,R_d$ to get the drain-source voltage V_{ds} as given by:

$$V_{ds} = V(N\Delta x) + I_d\,R_d \qquad (3.66)$$

Now the drain current and gate voltage (*i.e.* top gate voltage or back-gate voltage) characteristics are calculated for different values of drain-source voltages. Here, the given drain source voltage $V_{ds\text{-}const}$ is mentioned with the fixed parameters of Table-II and a condition is applied such that if drain source voltage by eq. (3.66) is same as the $V_{ds\text{-}const}$ then this current I_d is the desired current for the gate voltage. Such the I_d-$V_{gs\text{-}top}$ or I_d-$V_{gs\text{-}back}$ characteristics can be found. The necessary parameters of our proposed *GFET* are given here.

Table-I. The Parameters of our modeled graphene MOSFET

Parameters with Units	Parameters Values
$L(\mu m)$	5
$W\,(\mu m)$	1
$t_{ox\text{-}top}\,(nm)$	15
$t_{ox\text{-}back}\,(nm)$	285
$V_{gs\text{-}top,0}(V)$	1.45
$V_{gs\text{-}back,0}(V)$	2.70
$\rho_{sh,0}\,(cm^{-2})$	1.5×10^{12}
$R_s = R_d\,(\Omega)$	900
$n^*(cm^{-2})$	8×10^{11}
$\mu_p = \mu_n\,(cm^{-2}V^{-1}s^{-1})$	1500
$\hbar\Omega\,(meV)$	55

3.3 Modeling of ballistic top gated graphene MOSFET

3.3.1 Device Model

Top gated graphene MOSFETs as shown in Fig.1 were simulated. The simulated device has a top gate insulator thickness of t_{ins}=2 nm and dielectric constant of (H_fO_2)k_{ins}=9, which result in a gate insulator capacitance of C_{ins} = 3984 nF/cm^2 to minimize the gate electrostatic effect. No gate underlap is assumed, and the gate length is equal to the channel length L_g=L_{ch}=10 nm. The difference between the metal Fermi energy level and the Dirac point of graphene is E_F-E_D= −0.2 eV, which is typical for a high work function metal source or drain contact (such as Pd). The contact makes better contact for hole conduction as compared to electron conduction. Using the model shown in Fig. 1, the DC characteristics and RF performance of top-gate Graphene MOSFETs at ballistic limit is evaluated.
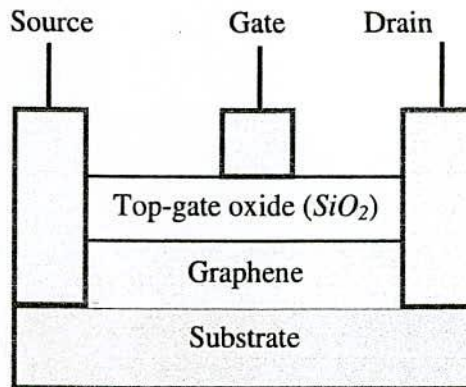

Fig.3.6: Cross section of the modeled top gate-graphene MOSFET

3.3.2 Non-Equilibrium Green's Function (NEGF)

MOS transistors with channel lengths as small as 10 nm are now being actively studied both theoretically and experimentally [37]. At the same time recent demonstrations of molecular switching make molecular electronic devices seem a little closer to reality [38]. It is clear that quantitative simulation tools for this new generation of devices will require atomic-level quantum mechanical models. The non-equilibrium Green function (NEGF) formalism (sometimes referred to as the Keldysh or the Kadanoff–Baym formalism) provides a sound conceptual basis for the development of this new class of simulators. 1D quantum devices like tunneling and resonant tunneling diodes have been modeled quantitatively using NEMO [39] which is based on the NEGF formalism. Although the transport issues in MOS transistors or molecular electronics are completely different, the NEGF formalism should provide a suitable conceptual framework for their analysis as well. However, this formalism is based on concepts that are unfamiliar to most device physicists and chemists and as such remains relatively obscure despite the obvious value of a fundamentally sound approach on which practical simulation tools for nanoscale devices can be based.

Most device physicists are familiar with the Schrödinger–Poisson solver. So let us start by recapitulating how the Schrödinger–Poisson solver works for a device in equilibrium (Fig. 3.7a).

The first step is to identify a suitable Hamiltonian H that provides an adequate description of the isolated device. For example, if the device operation involves only the electrons in a parabolic conduction band then we could use the effective mass Hamiltonian $H \equiv -(\hbar^2/2m)\nabla^2$.

Hamiltonian commonly used to provide an accurate description of the valence band. When the device is connected to the contacts there is some charge transferred into or out of the device, which gives rise to a potential, U(r) that has to be calculated self-consistently. The Schrödinger–Poisson solver (Fig. 1B) iterates between the Poisson equation which gives us the potential U(r) for a given electron density n(r).

$$\nabla^2 U(r) = \frac{-n(r)}{\in}$$

(3.67)

and the law of equilibrium statistical mechanics which tells us that the electron density n(r) for a given potential profile U(r) is obtained from

$$n(r = \sum_{\alpha} \left|\Psi_\alpha(r)^2\right| f_0(\varepsilon_\alpha - \mu)$$

(3.68)
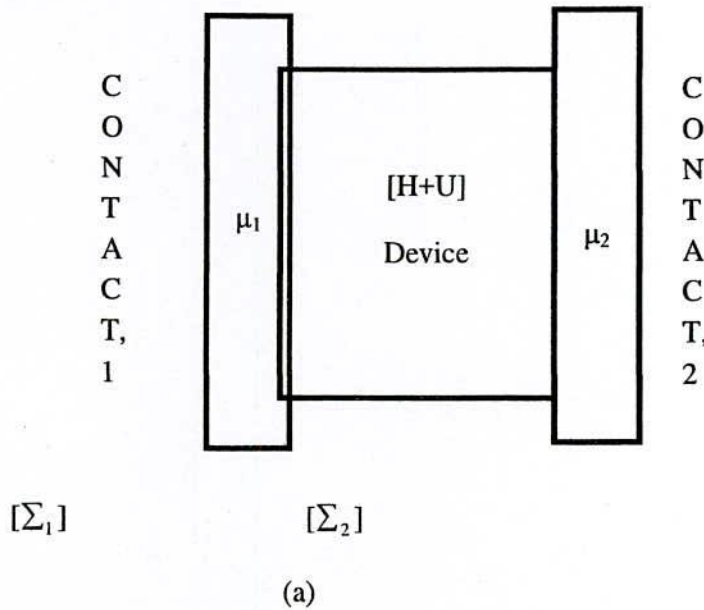
By filling the eigenstates $\Psi_\alpha(r)$ of the Schrodinger equation
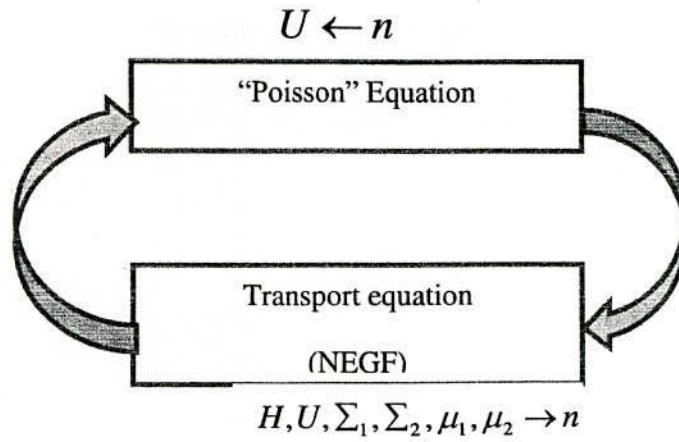
$$[H+U]\Psi_\alpha(r) = \varepsilon_\alpha \Psi_\alpha(r)$$

(3.69)

According to the Fermi function

$$f_0(E-\mu) \equiv (1+\exp[(E-\mu)/k_B T])^{-1}$$

(3.70)

μ being the Fermi level.

(a)

$$U \leftarrow n$$

| "Poisson" Equation |

| Transport equation |
| (NEGF) |

$$H, U, \Sigma_1, \Sigma_2, \mu_1, \mu_2 \rightarrow n$$

(b)

Fig. 3.7.(a) A device driven out of equilibrium by two contacts with different Fermi levels μ_1 and μ_2 (b)self-consistent procedure for determining the density matrix from which all quantities of interest (electron density, current etc.) can be calculated.

Periodic Boundary Conditions

The density matrix can be written as (I: identity matrix of the same size as [H_L])

$$[\rho] = \sum_k \rho_k = F_0([H_L - \mu I]) \tag{3.71}$$

We solve eqn (3.5) self-consistently with the Poisson equation

$$\frac{d^2 U}{dx^2} = \frac{q^2}{\varepsilon}[N_D - n] \tag{3.72}$$

using the standard finite difference method to write the Schrödinger equation on a discrete lattice we obtain

$$E\Psi_1 = -t\Psi_0 + (E_c + 2t + U_1)\Psi_1 - t\Psi_2 \tag{3.73a}$$

at the left end of the lattice. The problem is that we want to get rid of Ψ_0, in order to truncate [H_L] to a finite size. We have the same problem at the right end

$$E\Psi_N = -t\Psi_{N-1} + (E_c + 2t + U_N)\Psi_N - t\Psi_{N+1} \tag{3.73b}$$

where we would like to get rid of Ψ_{N+1}. If we simply truncate the matrix, we are in effect setting $\Psi_0 = \Psi_{N+1} = 0$ which makes the calculated electron density go to zero at the ends. This would be an appropriate boundary condition if we had an infinite potential wall at the ends. However, what we actually have is an open boundary and this is better described by periodic boundary conditions which effectively wrap the right end around and connect it to the left end by setting $H_L(1,N) = H_L(N,1) = -t$. The electron density then approaches the constant bulk value near the ends as we would expect. However, it is important to note that we are getting rid of end effects by artificially wrapping the device into a ring. We are not really doing justice to the open boundary that we have in the real device. The self-energy method that we will describe later in this section allows us to do that. But before we can describe this method, we need to discuss the Green's function approach for calculating the density matrix.

The density matrix can be written in the form

$$[\rho_k] = \int_{-\infty}^{+\infty} dE f_0(E + \varepsilon_k - \mu) \ \delta([EI - H_L])$$

$$[\rho] = \int_{-\infty}^{+\infty} dE F_0(E - \mu) \ \delta([EI - H_L]) \tag{3.74}$$

Using the standard expression for the delta function (0^+: positive infinitesimal)

$$2\pi\delta(x) = \text{Lim}_{\varepsilon \to 0^+} \left(\frac{2\varepsilon}{x^2 + \varepsilon^2}\right) = \frac{i}{x + i0^+} - \frac{i}{x - i0^+} \text{ we can write}$$

$$\delta(EI - H_L) = \frac{i}{2\pi}([(E + i0^+)I - H_L]^{-1} - [(E - i0^+)I - H_L]^{-1}. \tag{3.75}$$

Equations (3.8) and (3.9) can be rewritten in the form

$$[\rho_k] = \frac{1}{2\pi} \int_{-\infty}^{+\infty} dE f_0(E + \varepsilon_k - \mu)[A(E)]$$

$$[\rho] = \frac{1}{2\pi} \int_{-\infty}^{+\infty} dE F_0(E - \mu)[A(E)] \tag{3.76}$$

where $[A(E)]$ is known as the spectral function

$$[A(E)] = i([G(E)] - [G(E)]^+) \tag{3.77}$$

$[G(E)]$ being the retarded Green's function defined as

$$[G(E)] = [(E + i0^+)I - H_L]^{-1} \tag{3.78}$$

One can see from eqn (3.76) that the spectral function $[A(E)]/2\pi$ can be interpreted as the available density of states which are filled up according to the Fermi function to obtain the electron density. Indeed the diagonal elements of $[A(E)]/2\pi$ in the real space representation give us the local density of states at different points in space (a quantity that can be measured with scanning probe microscopy).
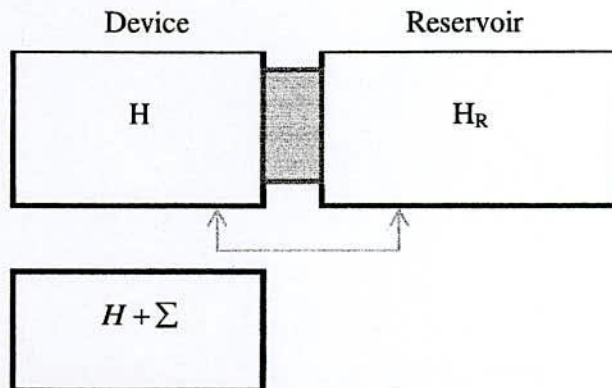

Fig. 3.8: The interaction of a device with a reservoir can be represented by a self-energy matrix Σ.

Self-energy

The concept of self-energy is used in many-body physics to describe electron–electron and electron– phonon interactions. In the present context, however, we are using this concept to describe something much simpler, namely, the effect of a semi-infinite contact. But the principle is the same. In general, we have a 'device' connected to a large reservoir and the overall Hamiltonian matrix has the form shown in Fig. 3.8 [40]

$$\begin{bmatrix} H & \tau \\ \tau^+ & H_R \end{bmatrix}$$

where the dimension of H_R is huge compared to that of H . The overall Green function has the form

$$\begin{bmatrix} G & G_{RD} \\ G_{RD} & G_R \end{bmatrix} = \begin{bmatrix} (E + i0^+)I - H & -\tau \\ -\tau^+ & (E + i0^+)I - H_R \end{bmatrix}^{-1}$$

We are only interested in G (and not in G_R, G_{RD} or G_{DR}), because we only care about the details inside the device and not inside the reservoir. It is straightforward to show that (see p. 146, Ref. [41])

$$G = [(E+i0^+)I - H - \Sigma]^{-1} \approx [EI - H - \Sigma]^{-1} \tag{3.79}$$

Where

$$\Sigma = \tau g_R \tau^+ \text{ and } g_R = [(E+i0^+)I - H_R]^{-1} \tag{3.80}$$

This shows that the effect of the coupling to the reservoir can be accounted for by adding a self-energy matrix Σ to the Hamiltonian H (Fig. 3.2). This is a very general concept that allows us to eliminate the huge reservoir and work solely within the device subspace whose dimensions are much smaller. Note that Σ is not necessarily an infinitesimal quantity (unlike 0^+); it can be finite with a value defined by the coupling to the reservoir. We will discuss the physical meaning of Σ further at the end of this section.

We could use eqn (3.80) in general to calculate the self-energy for arbitrary reservoirs and coupling matrices. It may seem that we have not gained much since we need to invert a huge matrix to obtain g_R which we need to evaluate the self-energy from eqn (3.80):

$$\sum(m,n) = \sum_{\mu,v} \tau(m,\mu)g_R(\mu,v)\tau^+(v,n)$$

The indices m, n refer to points within the device while μ, v refer to points inside the reservoir. However, the coupling matrix couples the points within the device to a small number of points on the surface of the reservoir, so that we only need $g_R(\mu,v)$ for points (μ,v) that are on the surface. This surface Green'sfunction can often be calculated analytically assuming a given model for the reservoir.

For the simple 1D problem at hand, the self-energy can be obtained from fairly elementary arguments without worrying about surface Green's functions. The self-energy matrix $\Sigma_1(E)$ that accounts for the semi-infinite lead on the left is given by ($t=\hbar^2/2ma^2$ as defined earlier before eqn (2.5))

$$\Sigma_1 = \begin{array}{cccc} |1| & |2| & \cdots & |N| \\ |2| & -t\exp(ik_1 a) & 0 & 0 \\ \cdots & 0 & 0 & 0 \\ |N| & 0 & 0 & 0 \end{array}$$

(3.81a)

Where $E = E_c + U_1 + 2t(1 - \cos k_1 a)$

In other words all we need is to add a term -t exp($i\, k_l a$) to $H_L(1,1)$ and we have accounted for the semi-infinite lead exactly, as far as calculating the Green's function is concerned. We can derive this result using an elementary argument. We stated earlier (see eqn (3.73a)) that the basic question at the boundary is how to eliminate Ψ_0 from the equation

$$E\Psi_1 = -t\Psi_0 + (E_c + 2t + U_1)\Psi_1 - t\Psi_2$$

With infinite wall boundary conditions we set Ψ_0 equal to zero while with periodic boundary conditions we set it equal to Ψ_N. In the self-energy method we assume that we only have outgoing (not incoming) waves at the ends. The fact that an actual device has incoming waves as well from the contacts is irrelevant when calculating G. G is the retarded Green's function representing the response of the system to an impulse excitation within the device: $[EI - H - \Sigma]G = I$, and hence the appropriate boundary condition for G is that we only have *outgoing* waves at the ends. This means that when calculating G we can write

$$\Psi_0 = \Psi_1 \exp[ik_1 a]$$

So that eqn(3.81a) becomes

$$E\Psi_1 = -t\exp[ik_1 a]\,\Psi_1 + (2t + U_1)\Psi_1 - t\Psi_2$$

showing that we can take care of the open boundary condition simply by adding a term -t exp[$i\, k_l a$] to point1, as stated above. Similarly the self-energy matrix $\Sigma_2(E)$ that accounts for the semi-infinite lead on the right has only one non-zero term at point N which is given by

$$\Sigma_2(N, N; E) = -t\exp(ik_2 a) \quad \text{where} \quad E = E_c + U_N + 2t(1 - \cos k_2 a)$$

(3.81b)

The Green's function is obtained from

$$G(E) = [EI - H_L - \Sigma_1 - \Sigma_2]^{-1}$$

(3.82)

where the self-energy functions $\Sigma_1(E)$ and $\Sigma_2(E)$ account for the open boundary conditions exactly. The spectral function A(E) is then obtained from eqn (3.8) from which the electron density is obtained using eqn (3.73). However, it should be noted that the periodic boundary conditions merely get rid of end effects through the artifact of wrapping the device into a ring while the self-energy method treats the open boundary condition exactly. An open system has a continuous energy spectrum, while a ring has a discrete energy spectrum. The electron density is obtained by integrating over energy and is relatively unaffected by the discretization of the spectrum at least at room temperature. But the difference would be apparent, if we were to look

at the density of states, that is, the spectral function. The full power of the self-energy method becomes apparent when we model a device under bias—a problem that cannot be handled with periodic boundary conditions.

Broadening

It might appear that the self-energy method is just another method for handling boundary effects. With infinite wall boundary conditions we set $\Psi_0 = \Psi_{N+1} = 0$; with periodic boundary conditions we set $\Psi_0 = \Psi_N$; in the self-energy method we set $\Psi_0 = \Psi_1 \exp[i\,k_1 a]$ and $\Psi_{N+1} = \Psi_N \exp[i\,k_2 a]$. However, there are two factors that distinguish $\Sigma_1(E)$ and $\Sigma_2(E)$ from ordinary Hamiltonians. Firstly, they are energy dependent. Secondly, they are not Hermitian. We can write

$$H_L + \Sigma_1 + \Sigma_2 = \left(H_L + \frac{\Sigma_1 + \Sigma_1^+}{2} + \frac{\Sigma_2 + \Sigma_2^+}{2} \right) + \left(\frac{\Sigma_1 - \Sigma_1^+}{2} + \frac{\Sigma_2 - \Sigma_2^+}{2} \right)$$

$$= \hat{H}_L - i\Gamma_1/2 - i\Gamma_2/2$$

Where $\Gamma_1 = i\left[\Sigma_1 - \Sigma_1^+\right]$, $\qquad \Gamma_2 = i\left[\Sigma_2 - \Sigma_2^+\right]$

The point we want to make is that the self-energy terms have two effects. One is to change the Hamiltonian from H_L to $\hat{H}_L$ which changes the eigenstates and their energies. But more importantly, it introduces an imaginary part to the energy determined by the 'broadening' functions Γ_1 and Γ_2. The former represents a minor quantitative change; the latter represents a qualitative change with conceptual implications.

One way to understand the meaning of these functions is to imagine a representation which diagonalizes H_L. This representation will not necessarily diagonalize Γ_1 and Γ_2—indeed interesting quantum interference effects often arise from the non-diagonal elements of Γ_1 and Γ_2. But if Γ_1 and Γ_2 are also simultaneously diagonalized then the eigenenergies of $(H_L + \Sigma_1 + \Sigma_2)$ will be given by

$$\varepsilon - i(\gamma_1 + \gamma_2)/2$$

Where ε, γ_1, and γ_2 are the corresponding diagonal elements of H_L, Γ_1 and Γ_2 respectively. This could be viewed as a broadening of the energy level from a delta function $\delta(E - \varepsilon)$ into a line of the form

$$\frac{\gamma_1 + \gamma_2}{(E-\varepsilon)^2 + \left(\frac{\gamma_1 + \gamma_2}{2}\right)^2}$$

which could have a non-Lorentzian shape since 1 and 2 are in general energy dependent. The imaginary part of the energy implies that the wavefunction and the associated probability decays with time which can be written in the form (neglecting any energy dependence of 1 and 2

$$\Psi \sim \exp\left[-\frac{i\varepsilon t}{\hbar}\right] \exp\left[-\frac{y_1 t}{\hbar}\right] \exp[-\frac{y_2 t}{2\hbar}]$$

$$|\Psi|^2 \sim \exp[-\frac{\gamma_1 t}{\hbar\hbar}]\exp[-\frac{\gamma_2 t}{\hbar}] \qquad (3.83)$$

An electron initially placed in that state will escape into the left and right leads with time constants $\hbar/\gamma_1$ and $\hbar/\gamma_2$ respectively. The quantities $\gamma_1/\hbar$ and $\gamma_2/\hbar$ thus represent the rates at which an electron initially in

(a)   (b)
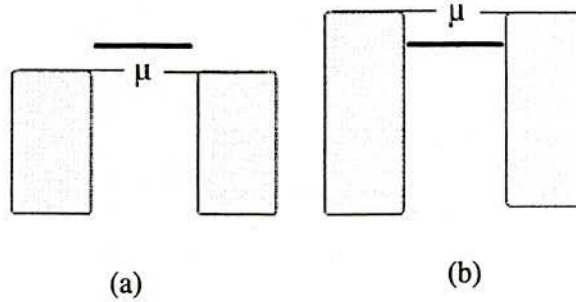
Fig. 3.9: A discrete level is coupled to a reservoir with a Fermi level μ. The broadening is the same regardless of whether the reservoir states are empty or filled. (a) Level coupled to empty states (b) level coupled to filled states.

particular state will escape into the left and right states respectively. For example, we have seen that a 1D lead gives rise to a self-energy that is purely diagonal in real space representation (see eqn (3.15a))

$$\Sigma(1,1) = -t\exp(ika) \rightarrow \Gamma(1,1) = 2t\sin(ka) = hv/a$$

which is quite reasonable since we expect the rate of escape from a lattice site of size 'a' to be v/a.

Coherent transport

We have seen in the last section that the equilibrium density matrix is obtained by filling up the available density of states (or spectral function [A])according to the Fermi function (see eqn (3.10)).
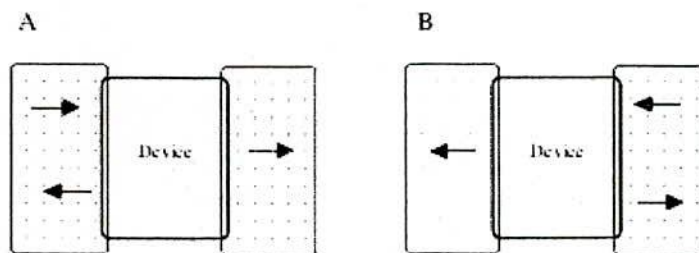

A   B

Fig. 3.10. The eigenstates of a composite contact–device–contact structure can be divided into two groups associated with incident waves from the A, left contact and; B, the right contact. If we neglect scattering processes under bias, then under bias the 'left' eigenstates in A remain in equilibrium with contact 1 (μ_1) and the 'right' eigenstates in B remain in equilibrium with contact 2 (μ_2).

The next problemis to find the density matrix if the device is connected to two contacts with different Fermi levels 1 and 2 (see Fig. 3), and hence different Fermi functions. The solution in general is quite involved: non-equilibrium statistical mechanics is a far more complex subject than equilibrium statistical mechanics. However, the answer is relatively simple, if we neglect scattering processes within the device (that is, if we assume transport to be coherent). This turns out to be a fairly accurate assumption for many ultra short devices like resonant tunneling diodes. The eigenstates of the composite contact–device–contact structure can then be divided into two groups associated with waves incident from the left and right contacts respectively (see Fig. 3.10). When a bias is applied, these 'left' eigenstates and 'right' eigenstates remain in equilibrium with the left contact and the right contact respectively. The ballistic conductor is a relatively simple example of this principle where the left eigen states are the '+k' states and the right eigenstaes are the '-k' states.

This simple observation (some might call it an ansatz) leads to an enormous simplification and is at the heart of the transmission formalism that is widely used in mesoscopic physics[40–42]. It allows us to treat a non-equilibrium problem using equilibrium statistical mechanics. At equilibrium, we fill up the full spectral function[A_1] according to the Fermi function. Under bias, we fill up part of it (the left spectral function [A_1]) according to the Fermi function in the left contact and part of it (the right spectral function [A_2]) according to the Fermi function in the right contact. The density matrix is given by (cf. eqn (3.10))

$$\rho_k = \int \frac{dE}{2\pi} [f_0(E + \varepsilon_k - \mu_1)A_1 + f_0(E + \varepsilon_k - \mu_2)A_2]$$

So that $\rho = \sum_k \rho_k = \int \frac{dE}{2\pi} [F_0(E - \mu_1)A_1 + F_0(E - \mu_2)A_2]$ (3.84)

The Green's function formalism provides a simple way to separate the total spectral function [A] into a left spectral function [A_1] and a right spectral function [A_2]:

$$A_1 = G\Gamma_1 G^+, \quad A_2 = G\Gamma_2 G^+ \tag{3.85}$$

$$G = [EI - H_L - \Sigma_1 - \Sigma_2]^{-1} \tag{3.86}$$

$$\Gamma_{1,2} = i\left[\Sigma_{1,2} - \Sigma_{1,2}^+\right] \tag{3.87}$$

We can prove that the total spectral function is indeed equal to the sum of the left and right spectral functions:

$$A \equiv i[G - G^+] = A_1 + A_2 = G\Gamma_1 G^+ + G\Gamma_2 G^2 \tag{3.88}$$

By writing equation (3.87) as

$$G^{-1} = EI - H_L - \Sigma_1 - \Sigma_2 \quad \text{and} \quad [G^+]^{-1} = EI - H_L - \Sigma_1^+ - \Sigma_2^+$$

$$\text{So that } G^{-1} - [G^+]^{-1} = i\Gamma_1 + i\Gamma_2$$

Premultiplying by G and post multiplying by G^+, we can prove eqn (3.20).

Current expression

An alternative expression for the current can be obtained from a rate equation point of view by writing the outflux from the device into contact 1 as [40]

$$I_{out} = (-q/h \int dE \text{trace}(\Gamma_1 \bar{\rho}) \tag{3.89}$$

which can be understood by noting that the density matrix is like the electron density while $01 = N h$ represents the rate at which electrons escape into the contact. The influx from the contact into the device can be written by equating it to the outflux we would have if the device were in equilibrium with that contact:

$$I_{in} = (-\frac{q}{h}) \int dE trace(\Gamma_1 \rho_1)$$

where

$$2\pi[\bar{\rho}_1(E) \equiv F_1[A_1(E)] + F_1[A_2(E)] \tag{3.90}$$

represents the density matrix we would have if F2 were equal to F1 . The net current is given by I D Iin Iout. Making use of eqns (3.87), (3.89)–(3.90) we obtain

$$I = (-q/h) \int dE \text{ trace}(\Gamma_1 A_2)[F_1 - F_2]. \tag{3.91}$$

We could go through a similar argument regarding the influx and outflux at the other interface to obtain an equivalent expression for the current:

$$I = (-q/h) \int dE \text{ trace}(\Gamma_2 A_1)[F_1 - F_2]. \tag{3.92}$$

Equations (3.91), (3.92) provide alternative expressions either of which can be used to calculate the terminal currents without explicitly calculating the density matrix.

Relation to the transmission formalism

An interesting aspect of eqns (3.91) and (3.92) is that the expression for the current has exactly the same form that is used in the transmission formalism [40]

$$I = (-\frac{q}{h}) \int dE T(E)(F_1 - F_2). \tag{3.93}$$

The function T . E / is typically interpreted as the probability that an electron will transmit from the left to the right contact. Equation (3.93) is often used to calculate the current in tunneling and resonant tunneling devices. Comparing eqn (3.93) with eqns (3.91), (3.92) it is clear that

$$T(E) = \text{trace}(\Gamma_1 A_2) = \text{trace}(\Gamma_2 A_1)$$

$$= \text{trace}(\Gamma_1 F \Gamma_2 G^+) = trace(\Gamma_2 G \Gamma_1 G^+) \tag{3.94}$$

The NEGF formalism, applied to a coherent device, can thus be viewed simply as a convenient method for evaluating the transmission probability. The basic physics is identical.

CHAPTER IV

4.1 Introduction

In this chapter the performance of dual gate large area graphene MOSFET is analyzed using analytical approach. Here we have used device length as 5 µm and width as 1 µm respectively. The detailed simulation results are given below.

4.2 C-V characteristics

The quantum capacitance as a function of gate voltage is investigated in this section. The effect of the quantum capacitance on the overall gate capacitance is also mentioned. The effect of the impurity concentration in the substrate layer is also considered. The quantum capacitance has a vital effect on the total DC characteristics as well as radio-frequency characteristics. Our simulation results using MATLAB are illustrated here.

From the beginning of our given model we investigate the effect of the quantum capacitance on the overall gate capacitance. We simulate this quantum capacitance by using the following data on the given table. Here a $3\ nmSiO_2$ top-gate dielectric, zero $V_{gs\text{-}top,0}$ and zero applied V_{ds} i.e. without feeding current into the model is considered. The effect of the impurity concentration n^* is taken into account. The value of the impurity concentration n^* is considered as $4\times10^{11}\ cm^{-2}$ as shown in Table−II:

Table-II: Different parameter symbol and values of Graphene MOSFET

Parameters symbol of GFET	Parameters value of GFET
$t_{ox\text{-}top}\ (nm)$	3
$C_{ox\text{-}top}\ (\mu Fcm^{-2})$	1.15
$V_{gs\text{-}top,0}\ (V)$	0
$n^*\ (cm^{-2})$	4×10^{11}
$V_{ds}\ (V)$	0
$v_F\ (cm\ s^{-1})$	1×10^8

The quantum capacitance and the potential across the quantum capacitance is solved by self-consistent method by using the values of Table−II.
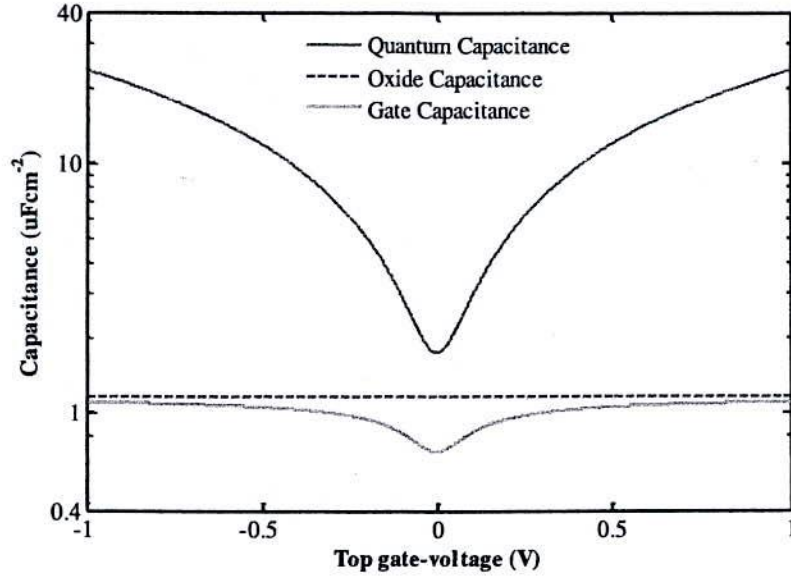
Figure 4.1: Quantum capacitance C_q(blue), top-gate oxide capacitance $C_{ox\text{-}top}$ (red) & gate capacitance C_g (green) of a graphene MOSFET structure as a function of top-gate voltage.

The minimum value of the quantum capacitance was found as 1.7325 μFcm^{-2} at zero top-gate voltage and the maximum value was found as 23.5009 μFcm^{-2} for both top-gate voltage $-1V$ and $+1V$ also at Fig. 4.1. The shape of the quantum capacitance is fully symmetrical on the both side of the Dirac point *i.e.* at the point where the minimum value of C_q is found.

4.3 Impurity Concentration Dependency of C_q

In this case we have used the value of the parameters as mentioned on Table-II. The quantum capacitance was shown for different values of the impurity concentrations n^* from 1×10^{11} cm^{-2} to 10×10^{11} cm^{-2} [35]. With the increasing value of n^* the minimum value of the quantum capacitance is also increased. But the shape of $C_q-V_{gs\text{-}top}$ curve is unchanged *i.e.* symmetrical with both the voltage-axis or the top-gate voltage. By taking different values of n^* from 1×10^{11} cm^{-2} to 10×10^{11} cm^{-2} the quantum capacitance C_q is found as shown below:

curves are about same shape with respect to both sides of the top-gate voltage axis. We can conclude that the impurity concentrations may affect more for the $C_{q,min}$ than the $C_{q,max}$ (for a given range of gate voltage). Though the $C_{q,min}$ is being changed then the gate capacitance is also being changed because C_g is related to C_q as a series combination of the C_{ox} and C_q. Impurity concentration has a great effect at $C_{q,min}$ or Dirac point [34].

4.4 Current Voltage (I-V) Characteristics

In our model we give the drain current as input and the corresponding drain-source voltage is found. But in this curve we simulate drain-current versus gate-voltage (*i.e.* top-gate or back-gate) for different fixed value of drain-source voltage (V_{ds}). For every iteration we set a fixed value of drain-source voltage (V_{ds}). Then according to the above procedure we calculate the drain-source voltage (V_{ds}) for a given range of drain current (I_d). In our total simulation the impurity concentration is considered as $n^* = 8 \times 10^{11}$ cm^{-2}. This value is considered through-out the total simulation of our model also.

The output characteristics from Fig. 4.3(a) deserve a closer inspection. While in the shown V_{ds} range the upper three curves for $V_{gs-top} = -3.0V, -2.25V, -1.50V$ and $-0.75V$ seemingly have a shape as known from conventional *FETs*, *i.e.* a linear region followed by a saturation of the drain current, the curve for $V_{gs-top} = 0.0V$ shows a kink-like shape with an inflection point followed by a subsequent increase in I_d (like a "second" linear region). First, I_d increases almost linearly with V_{ds}. Afterwards the drain current will saturate and reaches a plateau. Up to now the GFET behaves similarly to a conventional MOSFET. However, then a second increase of I_d is observed. This kink-like shape of the output characteristics is very distinctive for GFETs with large-area graphene channels and will now be examined in detail.

This behaviour arises from the transistors of p-type into n-type conduction at the drain end of the channel. It should be noted that at higher drain-source voltages the *I-V* curves for more negative gate voltages also show an inflection point. This behaviour occurs for a change in the conduction type at the drain end of the channel from p–type to n–type [25]. Fig. 4.3(a) and 4.3(b) shows the *I-V* characteristics of the graphene MOSFET for different V_{gs-top} at two back gate bias conditions, $V_{gs-back}$ of +40V and −40V respectively. Fig. 4.3(a) shows that the drain current I_d is increasing with increasing drain to source voltage V_{ds} for different top-gate voltages at constant back gate bias $V_{gs-back}=+40V$. The similar curves are displayed on Fig. 4.3(b) for $V_{gs-back}=-40V$ also. The drain current I_d as a function of drain-source voltage V_{ds} is illustrated for dual-gated large-area graphene MOSFET using the parameters as Table-I.
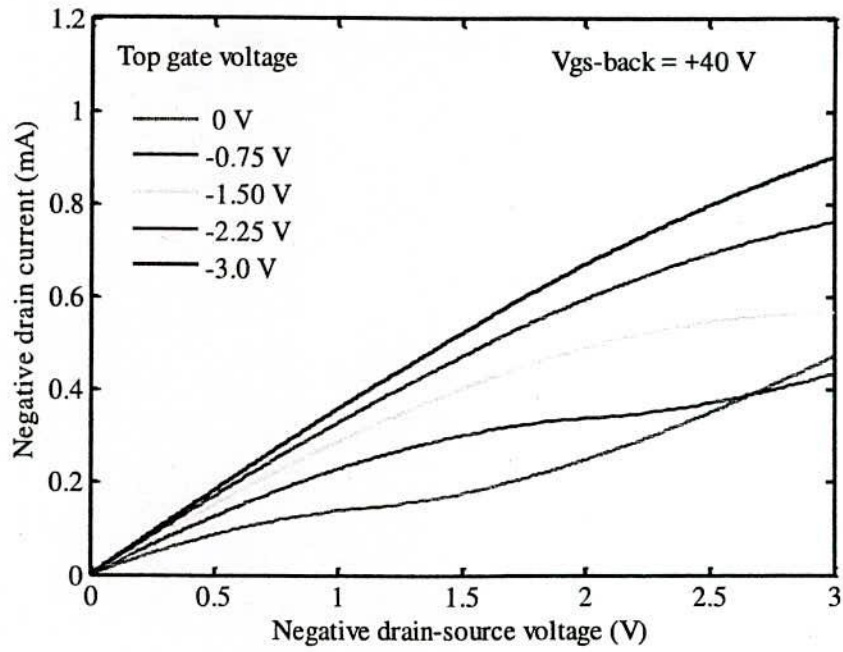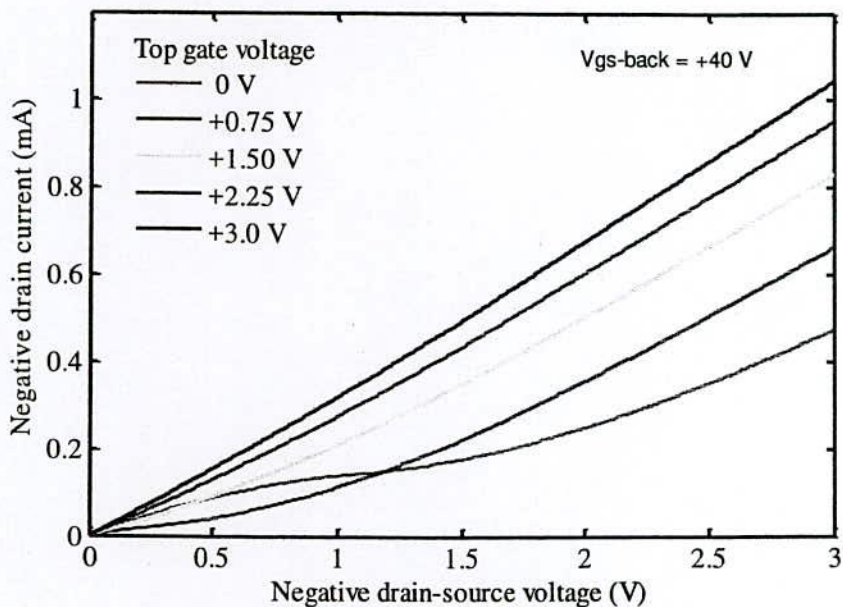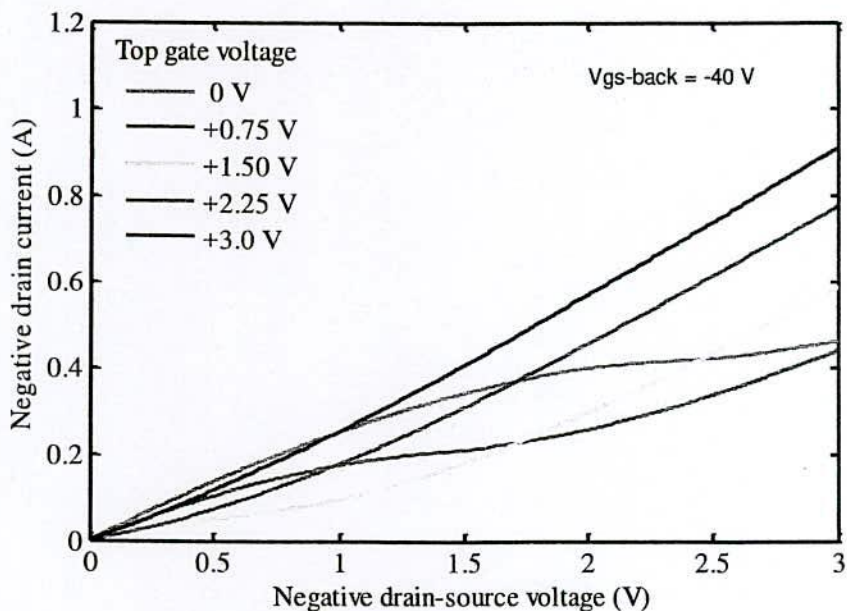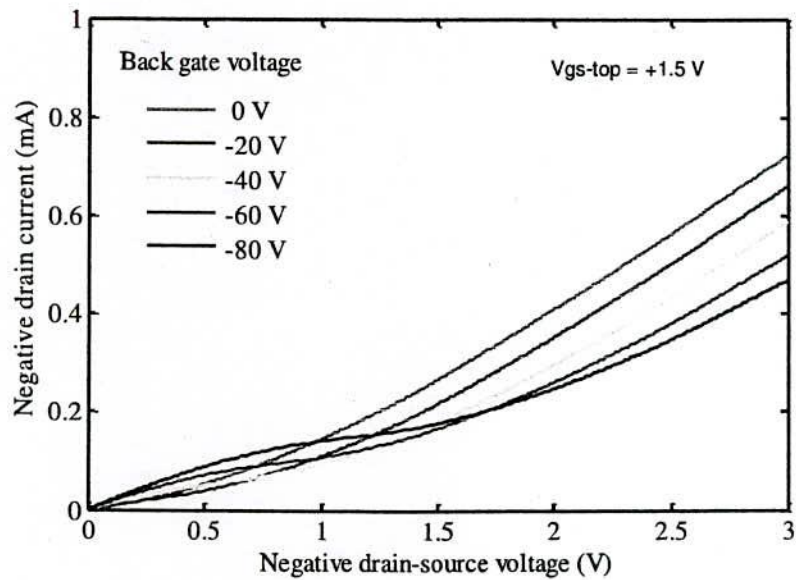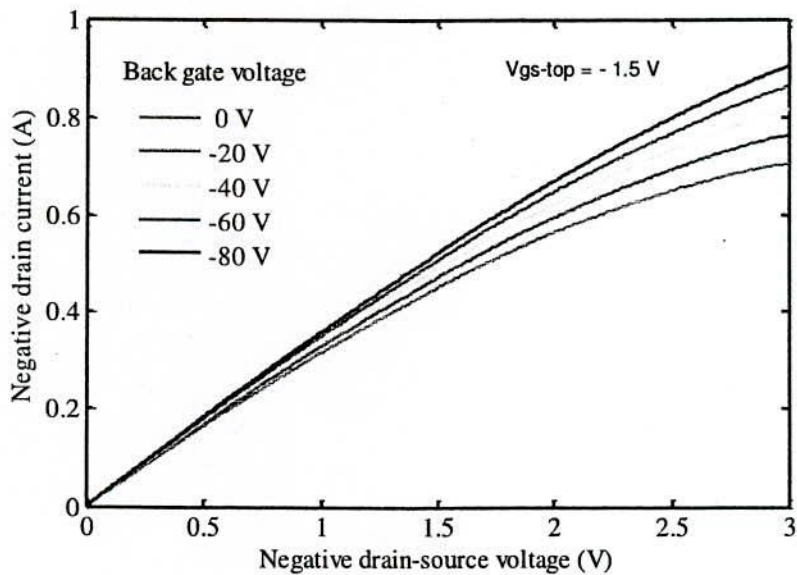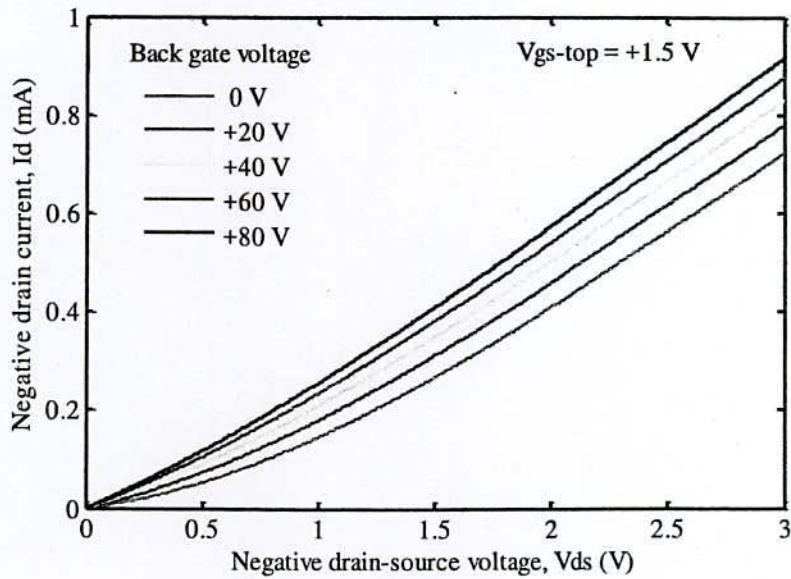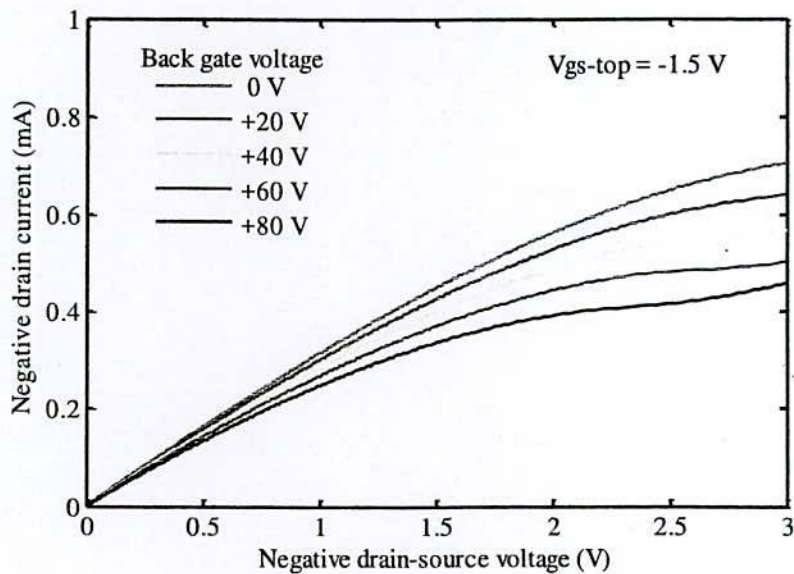
(a)
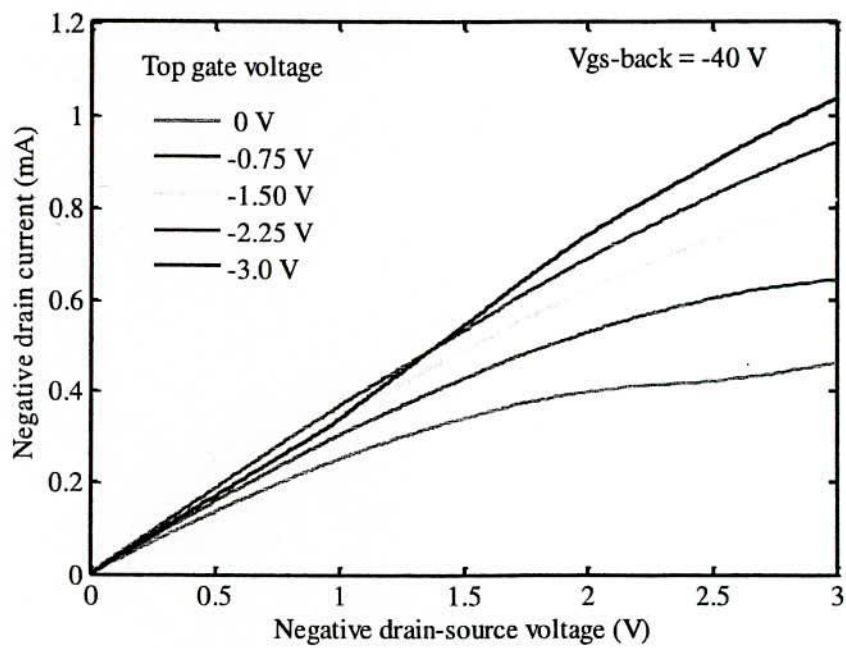
(b)

Figure 4.3: (a) The drain current I_d as a function of drain source voltage V_{ds} for five different values of V_{gs-top} at $V_{gs-back} = +40$ V. (b) The drain current I_d as a function of drain source voltage V_{ds} for five different values of V_{gs-top} at $V_{gs-back} = -40$ V.

The Fig. 4.4(a) and 4.4(b) show the *I-V* characteristics of the graphene MOSFET for different values of top-gate voltage V_{gs-top}= 0.0V, +0.75V, +1.50V, +2.25V and +3.0V for back-gate voltage $V_{gs-back}$ = +40V and −40V respectively.

(a)

(b)

Figure 4.4: (a) The drain current I_d as a function of drain source voltage V_{ds} for five different values of V_{gs-top} at $V_{gs-back}$ = +40 V. (b) The drain current I_d as a function of drain source voltage V_{ds} for five different values of V_{gs-top} at $V_{gs-back}$ = −40 V.

The Fig. 4.5(a) and 4.5(b) show the *I-V* characteristics of the graphene MOSFET for different values of back-gate voltage $V_{gs\text{-}back}$= 0.0V, −20V, −40V and−80V for top-gate voltage $V_{gs\text{-}top}$ = +1.5V and −1.5V respectively.

(a)

(b)

Figure 4.5: (a) The drain current I_d as a function of drain source voltage V_{ds} for five different values of $V_{gs\text{-}back}$ at $V_{gs\text{-}top}$ = +1.5 V. (b) The drain current I_d as a function of drain source voltage V_{ds} for five different values of $V_{gs\text{-}back}$ at $V_{gs\text{-}top}$= −1.5 V.

The Fig. 4.6(a) and 4.6(b) show the *I-V* characteristics of the graphene MOSFET for different back-gate voltages at two top gate bias conditions, of +1.5V and −1.5V respectively. Fig. 4.6(a) and 4.6(b) shows the transfer characteristics and it is seen that Dirac point shifts when the drain-source voltage is varied.

(a)

(b)

Figure 4.6: (a) The drain current I_d as a function of drain source voltage V_{ds} for five different values of $V_{gs-back}$ at V_{gs-top} = +1.5 V. (b) The drain current I_d as a function of drain source voltage V_{ds} for five different values of $V_{gs-back}$ at V_{gs-top} = −1.5 V.

(a)

(b)
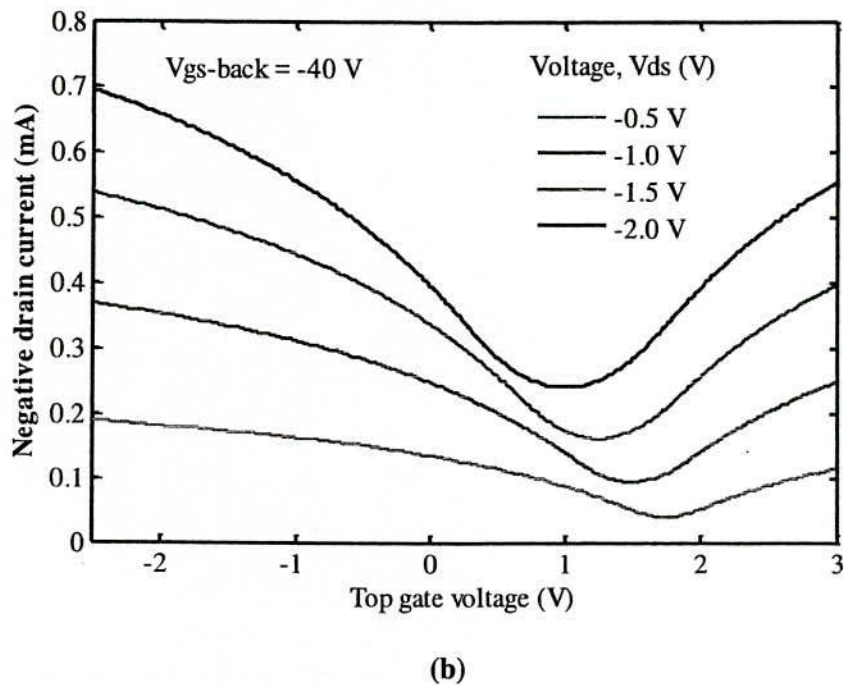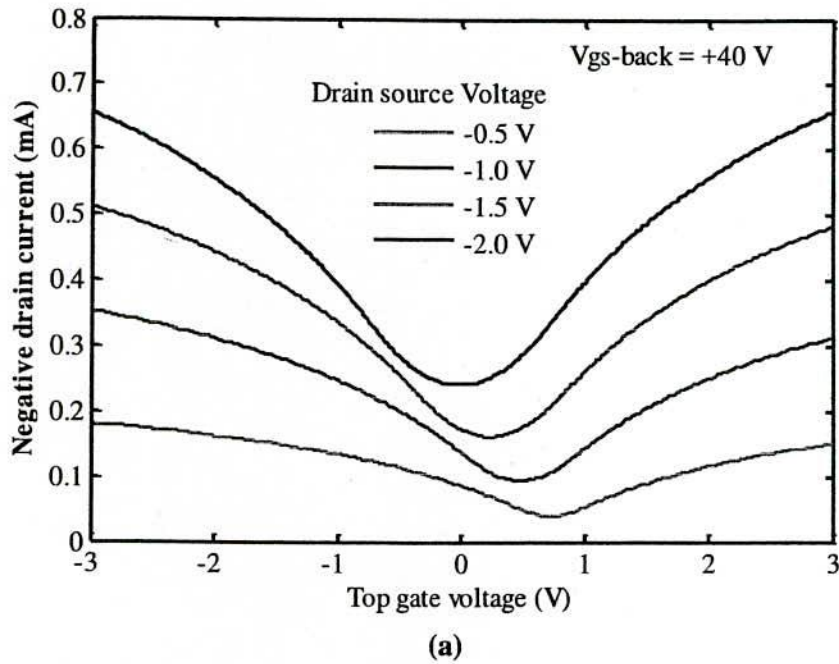
Figure 4.7: (a) The drain current I_d as a function of top-gate voltage $V_{gs\text{-}top}$ for four different values of V_{ds} at $V_{gs\text{-}back} = +40V$. (b) The drain current I_d as a function of top-gate voltage $V_{gs\text{-}top}$ for four different values of V_{ds} at $V_{gs\text{-}back} = -40V$.

The Fig. 4.7(a), 4.7(b) and 4.8show the transfer characteristics for different values of drain-source voltage V_{ds} are computed with the parameters from Table-I. In all curves the drain-current I_d is first decreasing with increasing $V_{gs\text{-}top}$ up to a certain point where it reaches a minimum and raises again forwards. This can be understood as follows: For zero $V_{gs\text{-}top}$ the majority charge

carriers are holes, since the energy bands are slightly up-shifted with respect to the Fermi energy, due to the back-gate voltage $V_{gs-back}$ of −40V.

If V_{gs-top} increases negatively, the channel potential will be lowered resulting in a smaller hole concentration. At the point, where V_{ch} is zero, i.e. $E_{C,V}= E_F$, the minimum carrier concentration is reached. A further increase of V_{gs-top} would result in a negative V_{ch} and therefore electrons would accumulate and over compensate the decrease of holes. Thus the current is increasing again. Such a behaviour involving both electrons and holes is called ambipolar. A qualitative explanation of why the minimum shifts with V_{ds} is observed. It can be seen that the Dirac point shifts when the drain-source voltage is varied. Such a shift is observed in experimental GFETs [33].
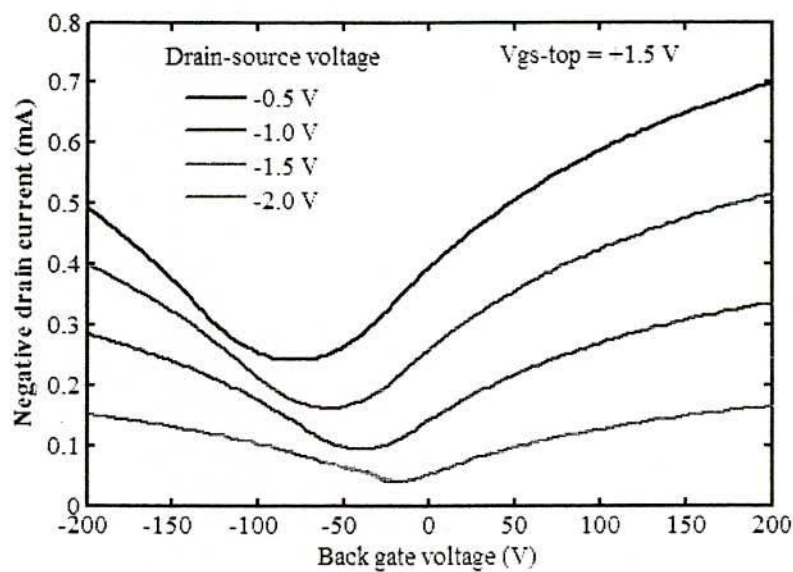

Figure 4.8: The drain current I_d as a function of back-gate voltage $V_{gs-back}$ for four different values of V_{ds} (−0.5V, −1.0V, −1.5V and −2.0V) at $V_{gs-top} = +1.5V$.

Kink Effect of I-V Curves

The variation of gate voltage directly affects the channel potential, V_x. The quantum capacitance, C_q and the graphene potential, V_{ch} are varied self-consistently with V_x which influences the sheet charge density, ρ_{sh}. Thus the drain current, I_d which is a function of gate voltage (V_{g-top} or V_{g-back}) and sheet charge density, ρ_{sh} is also changed. The I_d curve from Fig. 4.3(a) for $V_{gs-top}=0.0$ V, which shows a pronounced 'kink' in the characteristics signify the presence of an ambipolar channel. For our device in Fig. 3.1, with channel length L, $V(L)=V_{ds}$ so that for $V_{ds} \leq V_{ds-kink} \approx V_{gs-top}-V_0$, current is carried by holes throughout the length of the channel [5]. For $V_{ds} = V_{ds-kink}$, the vanishing carrier density produces a 'pinch-off' region at the drain that renders the current in the channel relatively insensitive to V_{ds} and results in the pronounced kink seen in the I–V characteristics. The $V_{ds}>V_{ds-kink}$, gives rise to an accumulation of electrons in the drain side and a

corresponding increase in the carrier density leading to a further increase in the drain current. Thus there produces an ambipolar regime in the graphene channel. The pinch-off point becomes a place of recombination for holes flowing from the source and electrons flowing from the drain. Because there is no band gap, no energy is released in this recombination [25].

4.4 Effects of Channel Potential

The parasitic series resistance (R_s) is considered for the following simulation curves by using MATLAB. But there may arise a question: Why channel potential is not start from the *0.0V* at the starting point of the source side? And this channel potential should be equal to the V_{ds} at the channel length *x=L*. Because $I_d R_s$ voltage is considered here at the source end.
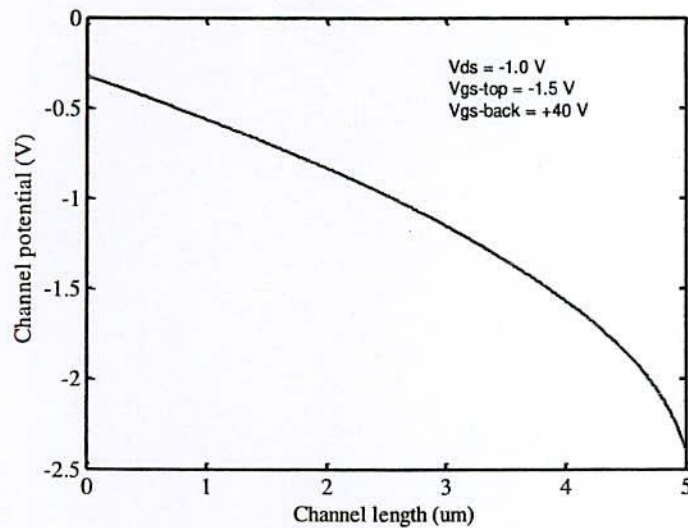

(a)
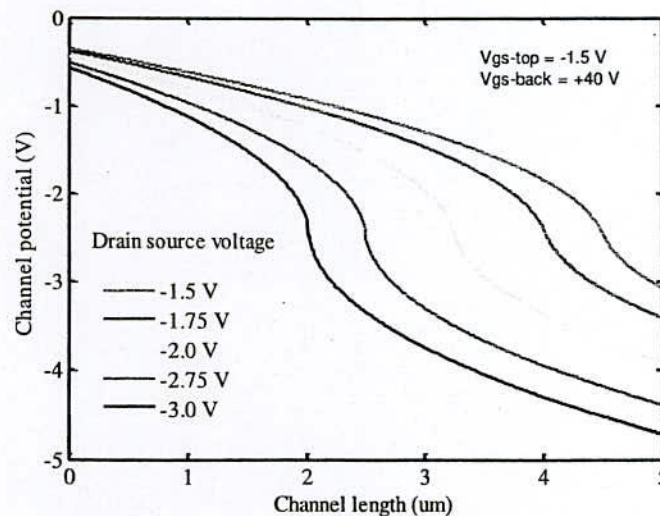
(b)

Figure 4.9: (a) The channel potential *V(x)* at $V_{ds}= -1.0V$ for $V_{gs-top} = -1.5V$ and $V_{gs-back} = +40V$.(b) The channel potential *V(x)* at $V_{ds}= -1.5V, -1.75V, -2.0V, -2.75V, -3.0V$ for $V_{gs-top} = -1.5V$ and $V_{gs-back} = +40V$.

Fig. 4.9(a) shows the simulation of potential on graphene channel with fixed $V_{ds} = -1.0V, V_{gs-top} = -1.5\ V$ and $V_{gs-back} = +40\ V$. At the source end *i.e.* at $x=0$, channel potential is zero. As the channel length increases the corresponding channel potential increases and becomes equal to drain voltage at the drain end voltage equal to $-1.0\ V$.

The graphene MOSFET structure having double gate, with series resistances while the remaining parameters are shown in Table-I. The Fig. 4.9(a) and Fig. 4.9(b) show the conditions in the channel for two different drain-source voltages V_{ds} of $-1V$ and five different values respectively. Let us start the discussion for an applied $V_{gs-top} = -1.5V$ and zero V_{ds}. Then the hole concentration is constant at any position in the channel and no current is flowing. If we gradually vary V_{ds} to $-1V$, an increasing current flows and the hole concentration at $x = L$ decreases for increasing absolute V_{ds}. At $V_{ds} = -1V$ the Fermi level at the source end of the channel ($x = 0$) is at $0\ eV$ and at the drain end ($x = L$) it is shifted downwards by $1\ eV$ due to V_{ds}. Thus, the local gate-to-channel voltage is $-1\ V$ at $x = 0$ and zero at $x=L$ as shown in Fig. 4.9(a). The bottom of the conduction band is shifted upwards by V_{ch} with respect to E_F at the source end of the channel, which results in a p-type (*i.e.*hole) conduction. At $x=L$, the bottom of the conduction band is located just at E_F -this corresponds to the Dirac condition, *i.e.* zero gate-induced carriers in the graphene and $\rho_{sh} = \rho_{sh0}$. We are now at the inflection point of the $I_d - V_{ds}$ characteristics.

If V_{ds} is further decreased to several values from $-1.5V, -1.75V, -2.0V, -2.75V$ and$-3.0V$ gradually (see Fig. 4.9(b)), we will obtain a positive gate-to-channel voltage of $+0.5\ V$ (for $V_{ds} = -1.5V$) at $x = L$. This gives rise to an accumulation of electrons and a corresponding increase in the carrier density leading to a further increase in the current. Now the majority charge carriers are holes at the source end of the channel and electrons at the drain end. In other words, ambipolar conduction occurs and the conductivity type of the channel changes between source and drain. Such a behavior is specific for GFETs, caused by the gapless nature of the channel due to the zero bandgap, and does not occur in conventional field-effect transistors. If we consider other values of V_{ds} for Fig. 4.9(b) the above explanation is true for all these conditions. These same criteria can applicable for Fig. 4.10(a) and 4.10(b) for sheet charge density; Fig. 4.11(a) and 4.11(b) for graphene potential; Fig. 4.12(a) and 4.12(b) for both $E_{c,v}$ and $V(x)$ respectively. From Fig. 4.9 to Fig. 4.12 it is very clear that the ambipolar conduction occurs at the channel of graphene *MOSFET*.

Fig. 4.10 (b) shows the variation of sheet charge density with channel length at different V_{ds}. As V_{ds} is decreased negatively the corresponding sheet charge density decreases up to Dirac point. After Dirac point we obtain a positive gate to channel voltage at the drain end which gives rise to an accumulation of electrons and corresponding increase in sheet charge density.
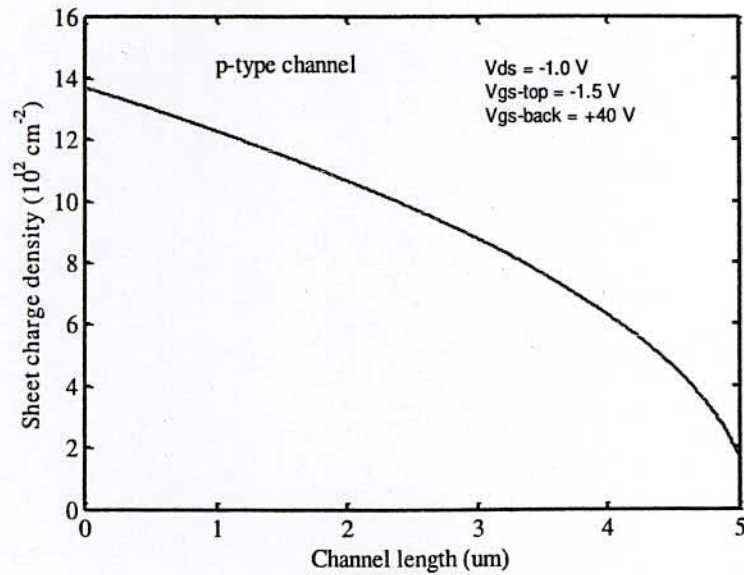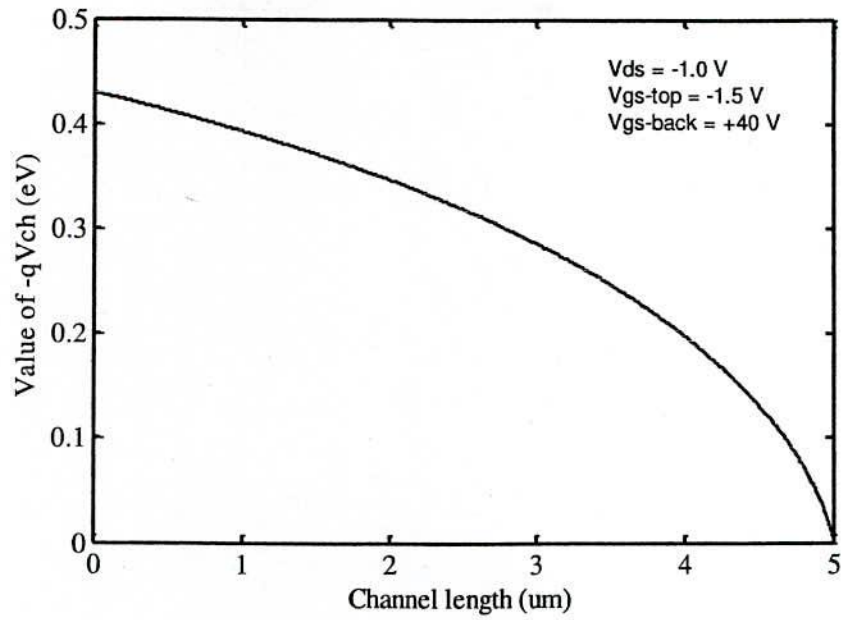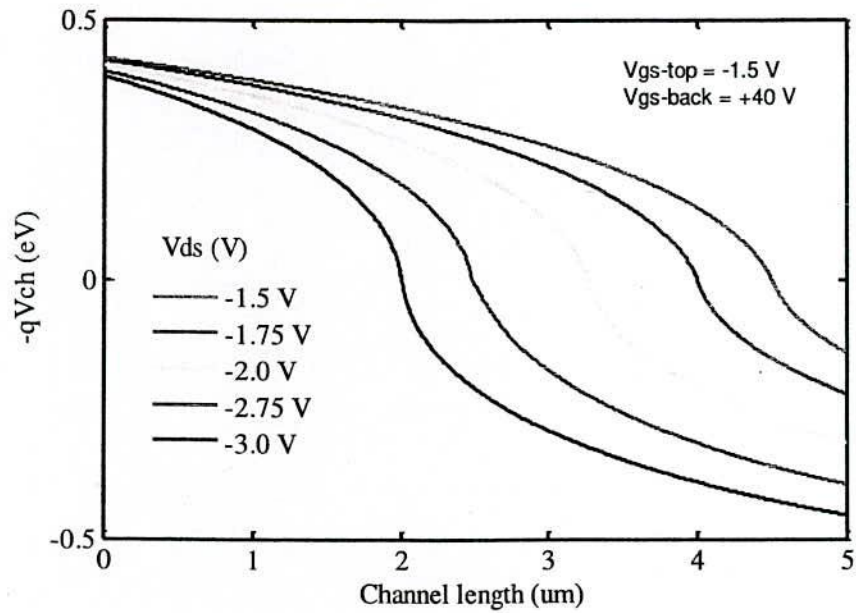

(a)
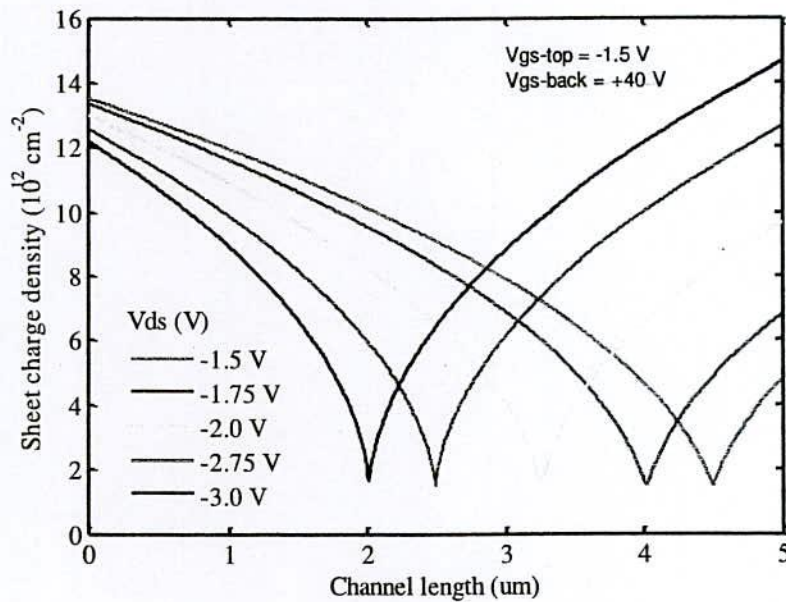
(b)

Figure 4.10: (a) The variation of the sheet charge density ρ_{sh} with channel length at $V_{gs\text{-}top}= -1.5\,V$, $V_{gs\text{-}back}=+40\,V$ with $V_{ds}= -1.0V$. (b) The variation of the sheet charge density ρ_{sh} with channel length at $V_{gs\text{-}top}= -1.5\,V$ and $V_{gs\text{-}back}=+40\,V$ with $V_{ds}= -1.5\,V$, $-1.75\,V$, $-2.0\,V$, $-2.75\,V$ and $-3.0\,V$.
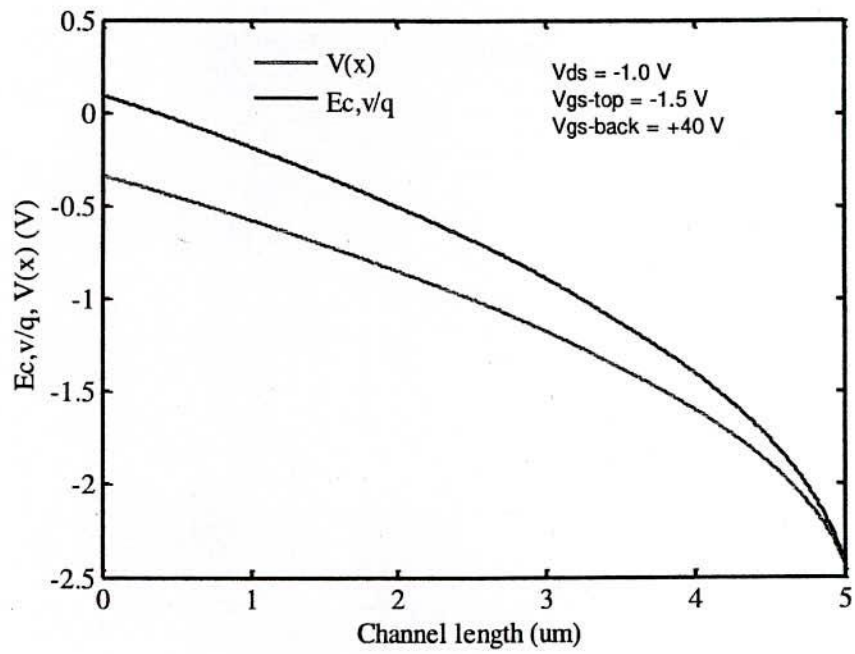
(a)

(b)

Figure 4.11:(a) The graphene potential qV_{ch} at $V_{ds} = -1.0V$ for $V_{gs\text{-}top} = -1.5V$ and $V_{gs\text{-}back} = +40V$.(b) The graphene potential qV_{ch} at $V_{ds} = -1.5V, -1.75V, -2.0V, -2.75V, -3.0V$ for $V_{gs\text{-}top} = -1.5V$ and $V_{gs\text{-}back} = +40V$.
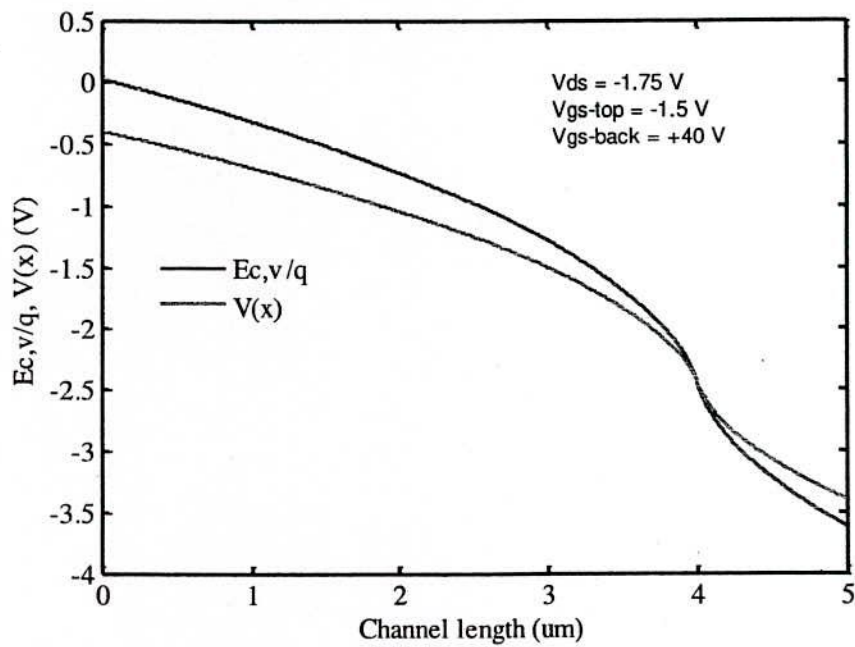
(a)

Figure 4.12:(a) The channel potential $V(x)$ and $E_{C,v}/q$ at $V_{ds} = -1.0V$ for $V_{gs\text{-}top} = -1.5V$ and $V_{gs\text{-}back} = +40V$. (b) The channel potential $V(x)$ and $E_{C,v}/q$ at $V_{ds} = -1.75V$ for $V_{gs\text{-}top} = -1.5V$ and $V_{gs\text{-}back} = +40V$.

4.6 Velocity Field Characteristics

The drift velocity and electric field is closely related to each other. In our simulation model we have the assumption to describe this effect also. With increasing values of electric field the drift velocity is also increased but after a certain range as the electric field is increased the drift velocity is not increased. Then drift velocity is limited to the average value of the Fermi velocity also. Fig. 4.13 shows the velocity-field relation for graphene MOSFET. It can be seen that the drift velocity increases linearly with the applied electric field and becomes saturated (2.12×107 cms-1) at 75.06 kV/cm similar to [45], [46].
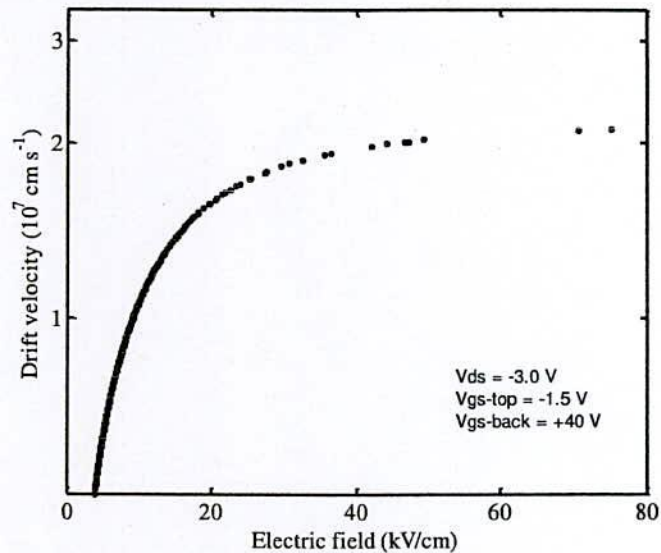
(a)
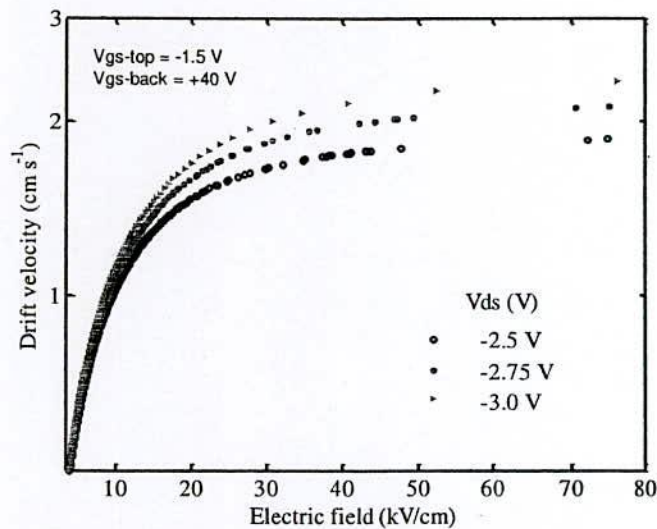
(b)

Figure 4.13: (a) The velocity-field relation for graphene MOSFET at $V_{gs\text{-}top}$= −1.5 V and $V_{gs\text{-}back}$= +40 V when V_{ds}= −3.0 V. (b) The velocity-field relation for graphene MOSFET at $V_{gs\text{-}top}$= −1.5 V and $V_{gs\text{-}back}$= +40 V when V_{ds}= −2.5V, −2.75V and−3.0 V.

CHAPTER V

Ballistic Top Gate Graphene MOSFET

5.1 Introduction

In this chapter the performance of a top gate graphene MOSFET in ballistic limit is analyzed using quantum transport simulation using NEGF formalism. Here we have used the device length as 10 nm. The detailed simulation results are given below.

5.2 Output I-V Characteristics

Fig. 5.1 shows the simulated drain current (I_d) as a function of drain voltage (V_{sd}) for different gate voltages. The I-V characteristics shows standard MOSFET type behavior along with the high drain current density reaching to ~12000 μA/ μm which is promising. The reason for the high current density can be attributed to the light effective mass of graphene and high carrier velocity [45].

As the FET is biased in the saturation regime, the average carrier injection velocity at the source end of the device is found to remain almost constant with regard to the applied gate voltage over a wide voltage range, which results in significantly improved transistor linearity compared to what a simpler model would predict. Physical mechanisms for good linearity are explained, showing the potential of graphene FETs for analogue electronics applications [46].
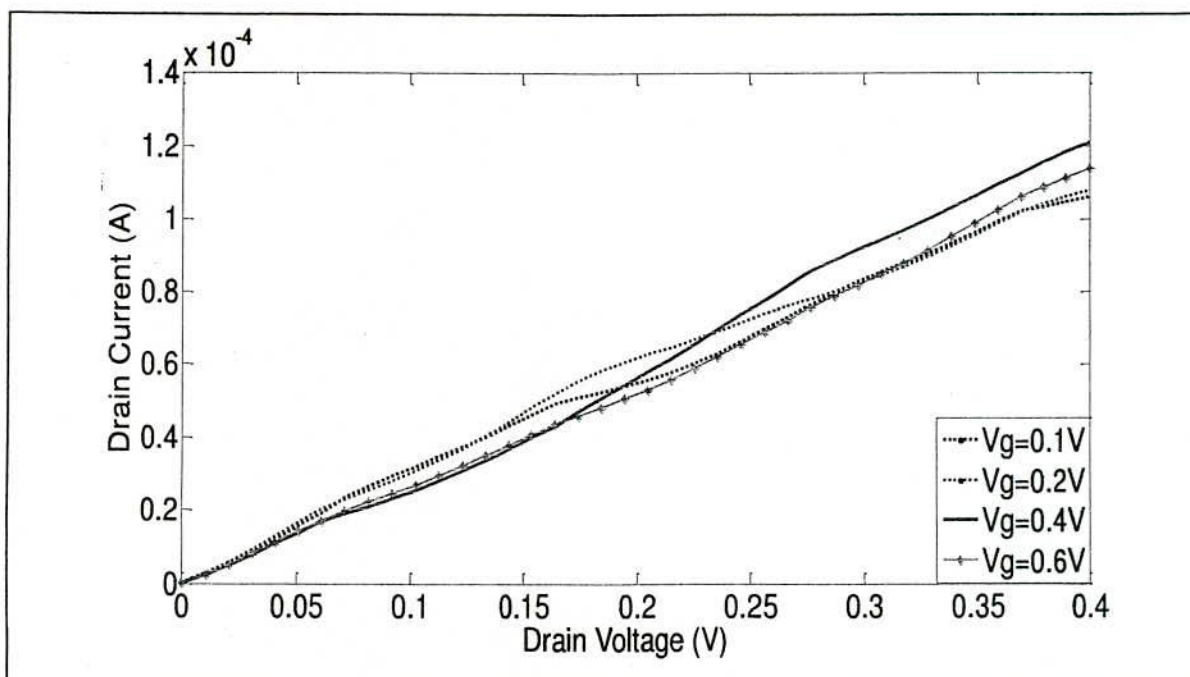

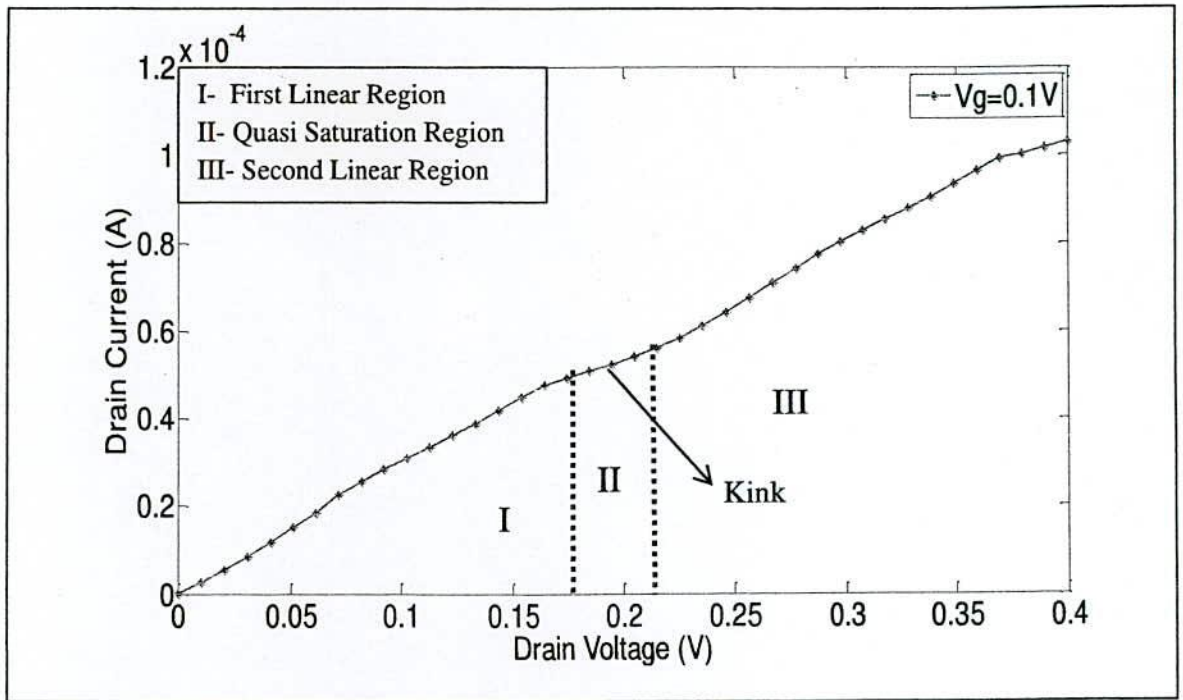Fig. 5.1 I-V Characteristics of a top-gated graphene MOSFET

Fig. 5.2 I_D–V_{SD} Characteristics of graphene MOSFET.

At lower gate voltage, ($V_g \leq 0.2$) a pronounced 'kink' is observed in drain current characteristics. At higher gate voltage ($V_g \geq 0.4$) this kink effect almost disappears. At a gate voltage, V_g=0.1V, there observed a significant 'kink' which is shown more details in Fig. 5.2.

It is observed there are three regions in I_D–V_{SD} characteristics shown in Fig. 5.2 such as First Linear Region (I), Quasi Saturation Region (II), Ambipolar Region(Second Linear Region, III).

I. First Linear Region:

In the first linear region, the drain current is carried by holes throughout the length of the channel which is shown in the Fig. 5.3(I)

II. Quasi Saturation Region: At a lower gate voltage there produces a kink in the drain current characteristics which was first reported in simulated and experimental results [47], [48].

For Vsd=Vsd-kink, the vanishing carrier density produces a 'pinch-off' region at the drain (Fig. 5.3, II) that renders the current in the channel relatively insensitive to Vsd and results in the pronounced kink seen in the I–V characteristic [49]. This region is called unipolar or Quasi-saturation region. Although the channel saturates at Vsd=Vsd-kink, the drain end of the channel may not experience charge neutrality at this potential. This quasi saturation behavior is due to the drain Fermi level aligning with the Dirac point profile in the channel, followed by the onset of ambipolar regime. The low density of states around the Dirac point gives rise to decrease in

current increment and explains the saturation observed for voltages where drain Fermi level is in vicinity of conduction band in channel. Since the density of states is low only in a very small energy range around Dirac point, graphene MOSFETs do not exhibit complete saturation seen in conventional silicon MOSFETs. The length of the Quasi-saturation region is dependent on the Fermi level. At a gate voltage Vg = 0.1 and 0.2 V a visible quasi-saturation region is noticed, where at Vg = 0.4 and 0.6 V the Quasi-saturation saturation region almost disappears.

III. Ambipolar Region (Second Linear Region):

An additional increase in the drain voltages beyond $V_{sd-kink}$, i.e. for Vsd>Vsd-kink the charge neutrality point is pushed into the deeper of the channel, toward the source (Fig. 5.3, III). As a result, electrons are injected into the channel from the drain end. These electrons are mobile rather than having depleted region between the point of pinchoff and the drain terminal with fixed negative charges. This is as a result of a zero bandgap in 2-D bilayer graphene, and the phenomenon is known as ambipolar transport [49]. In this bias range the carriers in the channel on the source side of the dirac point are holes, and those on the drain side are electrons. In this ambipolar regime, the pinch-off point becomes a place of recombination for holes flowing from the source and electrons flowing from the drain. No energy is released in this recombination due to absence of bandgap. In this region, the channel conduction is carried out by both electron and holes so it is called ambipolar region. However, in the ambipolar saturation region, the drain current increases with an increase in the drain voltage, and this behavior has been referred to as a second linear region [52] as shown in Fig. 5.2, III.
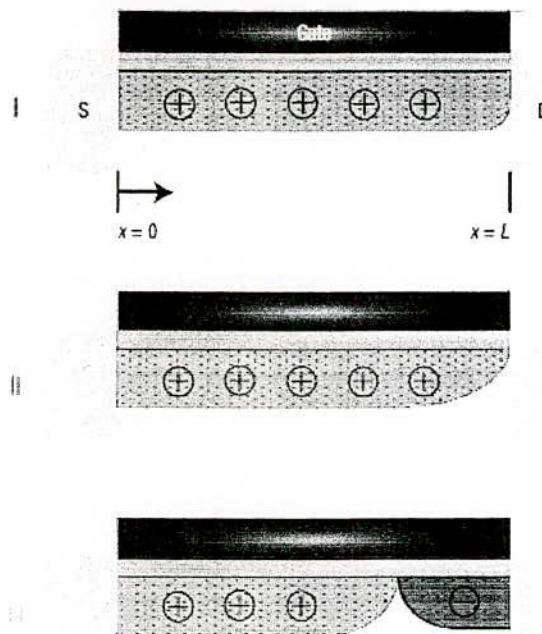

Fig. 5.3 Schematic demonstration of the carrier concentration under the top gate region. At point I ($V_{sd} < V_{sd-kink}$), the channel charge at the drainend begins to decrease as the minimal density point enters the channel. At point II ($V_{sd} = V_{sd-kink}$), the minimal density point forms at the drain. For $V_{sd} > V_{sd-kink}$ (point III), an electron channel forms at the drain [47].

5.3 Transfer Characteristics:

Fig. 5.4 (a) and (b) shows the calculated transfer characteristics of a top gated graphene MOSFET. It can be seen that the dirac point shifts when the drain-source voltage is varied. It is noticed that dirac point voltage, V_{dirac} shifts significantly towards right from 0.4 to 0.6V at positive drain bias shown in Fig. 5.4(a). This is due to the change of channel conductivity from p type to n type. Where as V_{dirac} shifts slightly towards left from 0.25 to 0.15V at negative drain bias shown in Fig. 5.4(b). So, the shift of dirac point voltage V_{dirac} in positive drain bias is more prominent than negative drain bias. Also, the p-n asymmetry is due to short channel effect.
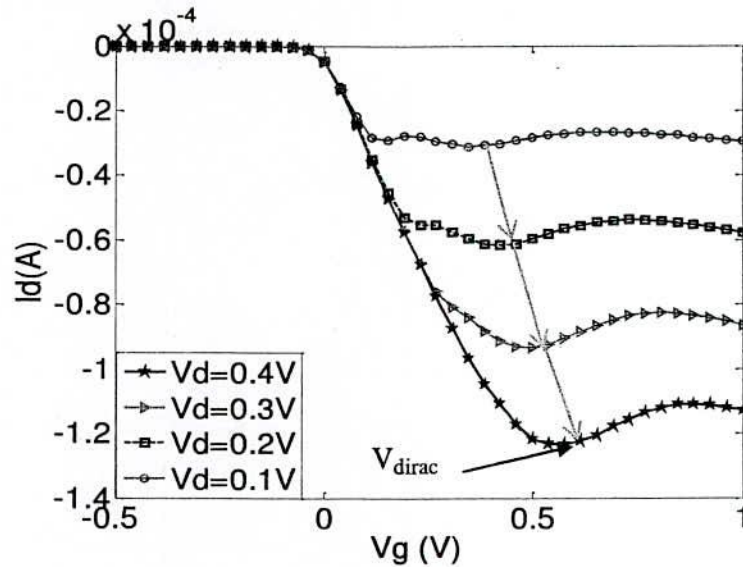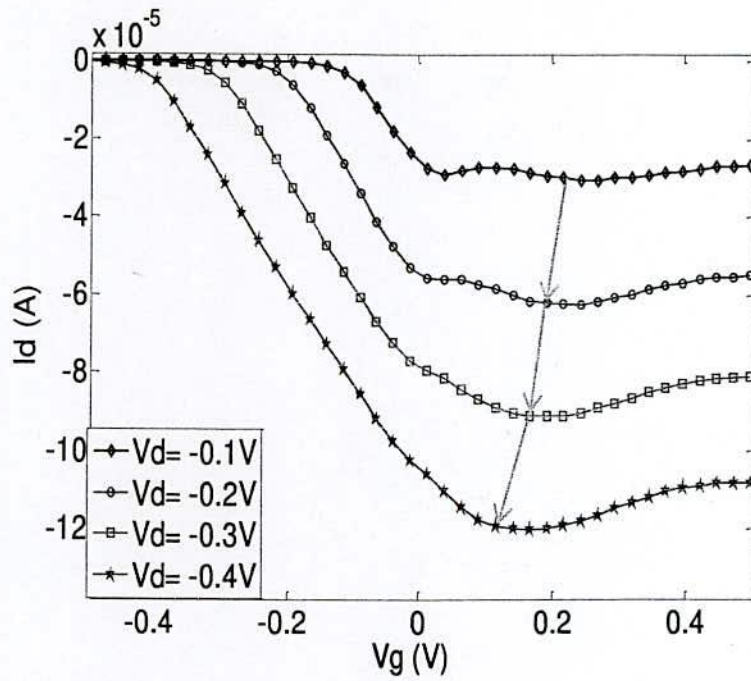

Fig. 5.4 (a) $I_d - V_g$ curve for top gated graphene MOSFET at positive drain bias.

(b)

Fig. 5.4 (b) $I_d - V_g$ curve for top gated graphene MOSFET at negative drain bias.

5.4 Tranconductance characteristics

Fig. 5.5 shows the variation of transconductance with the gate voltage. The maximum simulated transconductance for ballistic condition is $g_m \approx 4500 \ \mu s/\mu m$ at $V_g=0.07V$ which leads to high cut-off frequency for Graphene MOSFET. With increasing gate bias the corresponding transconductance decreases.
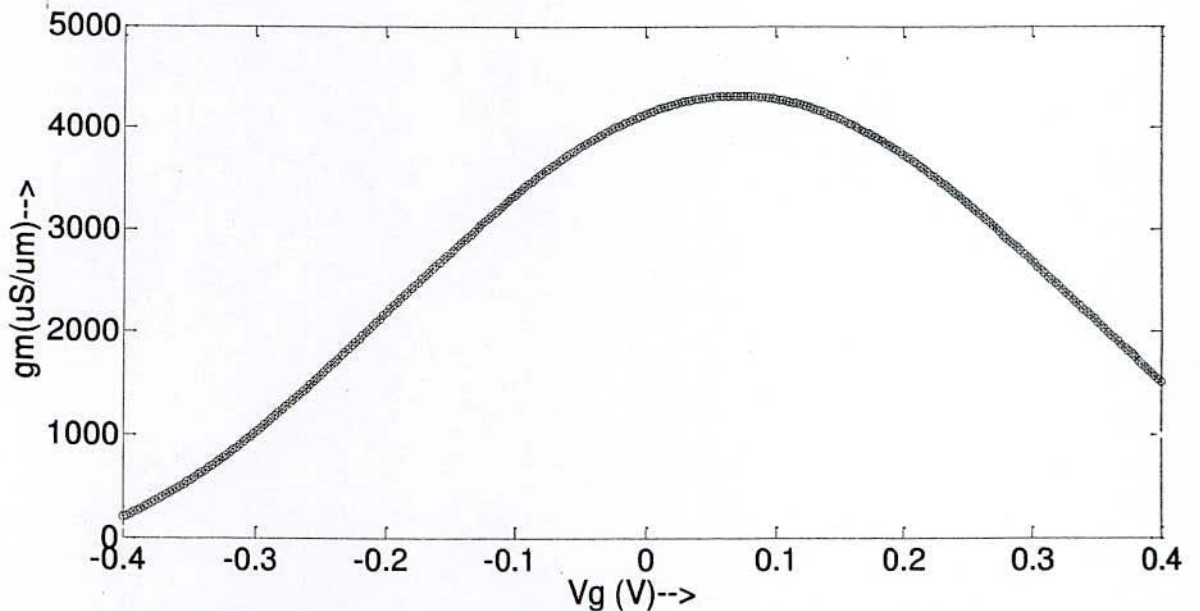

Fig.5.5   Transconductance, g_m vs Gate voltage, V_g of a top-gated graphene MOSFET

Next part focuses on studying scaling of small signal parameters such as transconductance with the channel length under ballistic conditions. Fig. 5.6 shows the variation of transconductance with channel length varying from 10 nm to 80 nm. The output transconductance, g_m, increases with the decrease of the channel length as shown in here. The decrease in transconductance is becoming more prominent at longer channel lengths.
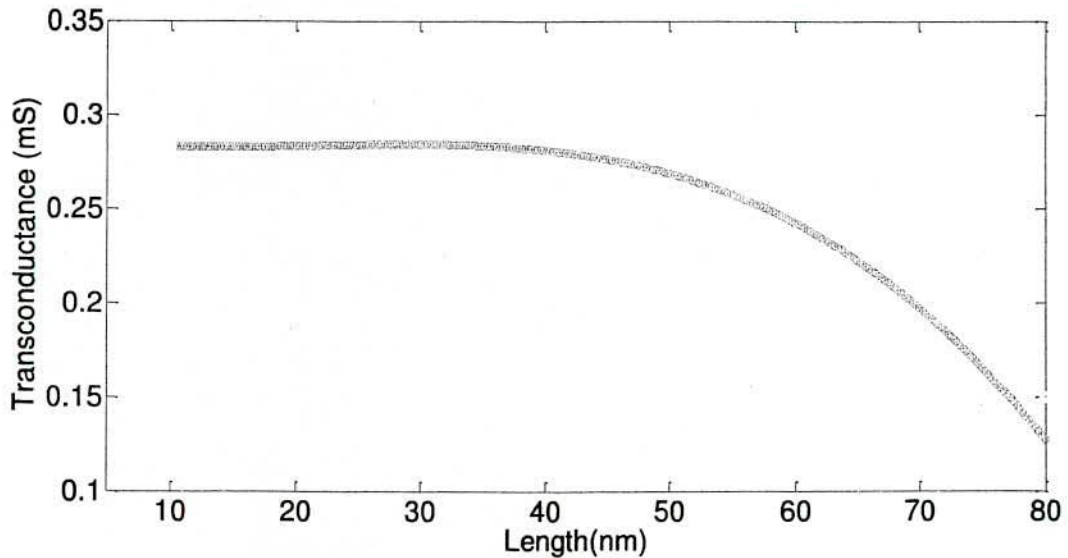

Fig.5.6.Transconductance, g_m vs Length of a top-gated graphene MOSFET

Fig. 5.7 shows the output transconductance, g_{ds},as a function of the channel length. As the channel length scales from 80 nm to 50 nm, the ballistic output transconductance increases only very slightly. As the channel length scales down to 50 nm the output transconductance, g_{ds}, however, rises significantly due to electrostatic gate effect. At short channel length (10-40 nm) the transconductance becomes constant that helps to keep the constant cut-off frequency in short channel lengths.
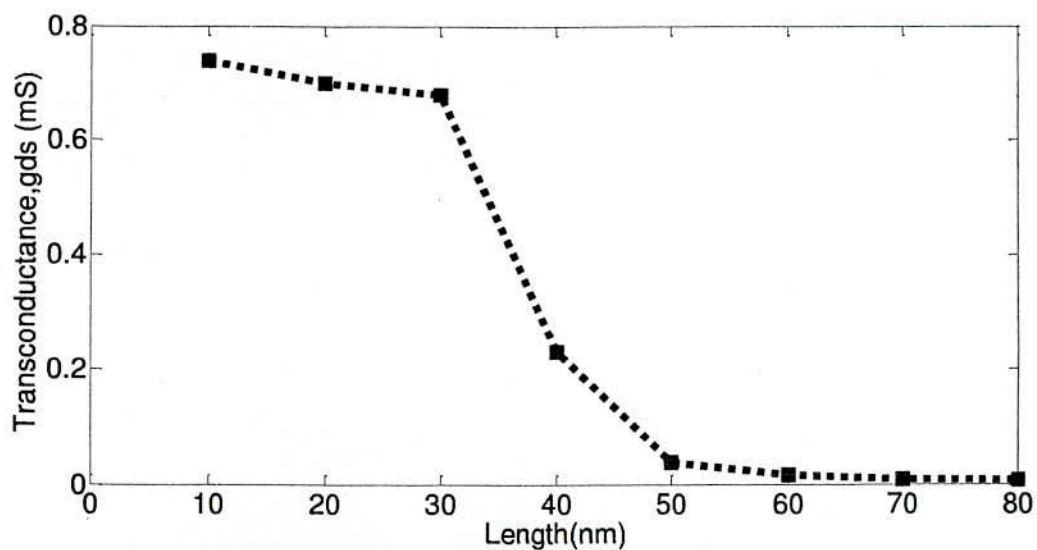

Fig.5.7. Drain Transconductance, g_{ds} vs Length of a top-gated graphene MOSFET.

5.5 Dependence of Fermi energy on gate voltage and density of states (DOS)

Fig. 5.8 displays the dependence of Fermi energy, E_f on gate voltage, V_{TG} for three different values of Cg. As expected, an increase of $|Ef|$ with increasing $|VTG|$ is observed. This effect is strong at small voltages. Close to $VTG = 0$, a linear behavior is observed leading to a large increase in E_f for small changes of VTG. The (unphysical) saturation portion indicated in Fig.5.8 is due to the dominating cable capacitance. The Density of States (DOS) which is directly proportional to quantum capacitance is a function of Fermi Energy. Here the DOS is plotted against Fermi Energy for different oxide capacitance (Cg).
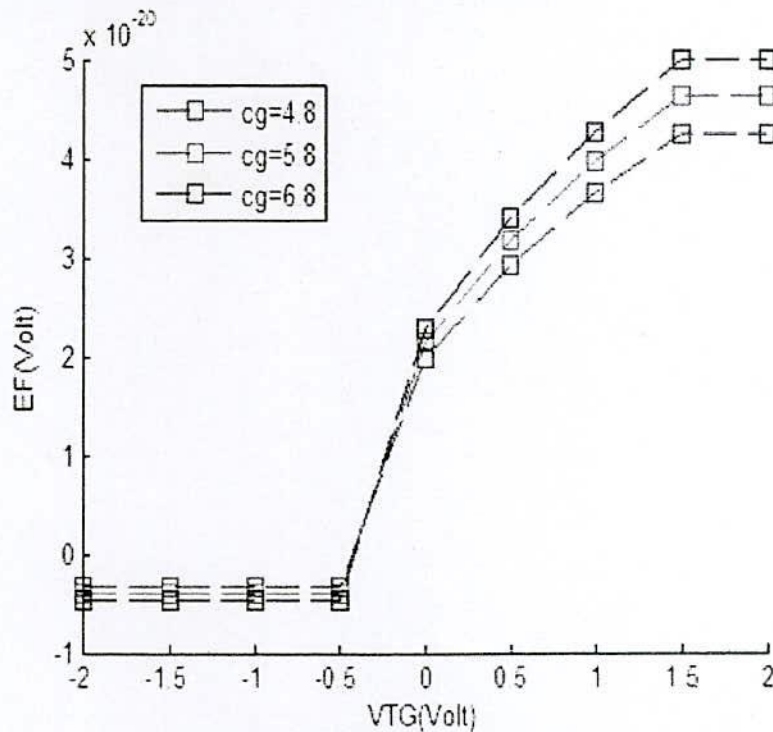

Fig. 5.8 Gate voltage (*VTG*) vs Fermi Energy (*E$_f$*) curve for different Cg

Fig. 5.9 represents the DOS vs E_f curve for ideal graphene given by equation. $D(E_f) = \dfrac{2E_f}{(\pi v_f \hbar)^2}$).Here, the variation of DOS with respect to E_f is linear. DOS at the Dirac point is zero.
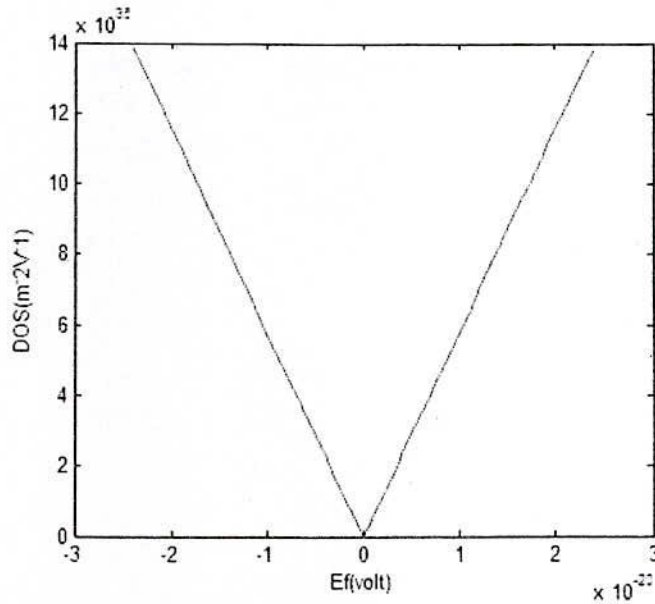
Fig. 5.9: Density of states as a function of Fermi energy for ideal case

Fig. 5.10 depicts that the value of DOS at the charge neutrality point (Dirac point) is non zero which is not identical with the theoretical density of states for ideal graphene shown in fig. 5.9. In contrast to theory, there is a finite number of states close to the charge neutrality point. This is due to the presence of local potential variations within the graphene sheet.

Fig. 5.10: Density of states as a function of Fermi energy for different oxide capacitance

CHAPTER VI

Conclusions and Recommendations

6.1 Conclusions

In this dissertation, the theoretical performance of graphene MOSFET is studied in large area and ballistic limit. In case of simulating large area graphene MOSFET, an analytical approach is applied. On the oth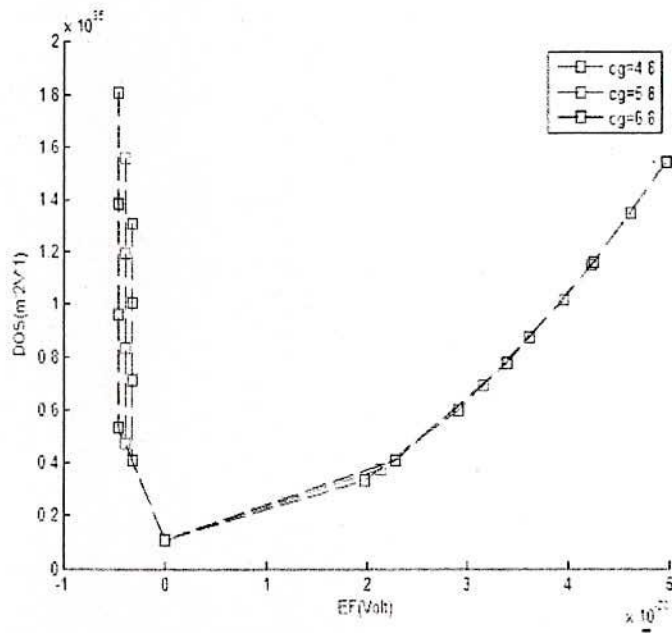er hand the performance of graphene MOSFET in ballistic limit is evaluated using quantum transport simulation based on the NEGF formalism.

We have calculated sheet charge density dependent quantum capacitance self consistently considering charged impurities in the gate oxide. With increasing charged impurities concentration the quantum capacitance increases near the Dirac point. A maximum value of quantum capacitance 23.564 μFcm^{-2} is obtained at $V_{gs-top}= \pm 1V$ with the chargedimpurities concentration of 8×10^{11} cm^{-2}. The linear channel potential profile is also evaluated.

The effects of dual gate voltage on the I-Vcharacteristics of graphene MOSFET is illustrated here. The double gate provides superior control of short channel effects and higher currents compared to a single gate MOSFET. The kink-like shape of the output I-V characteristics with large-area graphene MOSFET is observed. In large area graphene it is found that current conduction is occurred by electron or hole or combination of both depending on the drain bias which is the proof of the ambipolar nature of graphene channel.

The transfer characteristics show the p-n symmetry with respect to minimum conductivity point or dirac point in the large area graphene channel. The dirac point shifts towards right with increasing drain bias negatively. High saturation velocity is obtained along with high drain current. The sheet charge density profile decreases up to Dirac point (minimum conductivity point) as drain bias is decreased negatively. After Dirac point we obtain a positive gate to channel voltage at the drain end which gives rise to an accumulation of electrons and corresponding increase in sheet charge density.+

In the ballistic limit, the performance of a top gate graphene MOSFET with 10 nm channel length is simulated. The current–voltage characteristics of the device is computed. The resulting high drain current density ~12000 $\mu A/\mu m$ indicates high on-current for GMOSFETs. The shift of dirac point voltage V_{dirac} in positive drain bias is more prominent than negative drain bias. Also the p-n asymmetry in transfer characteristics is the signature of short channel effect. The output transconductance of the device is obtained in the range of ≈ 4500 $\mu S/\mu m$ which is very much promising for high speed nano transistors.

The output tansconductance, g_m, increases with the decrease of the channel length. The decrease in transconductance is becoming more promiminent at longer channel lengths. On the other hand, as the channel length scales from 80 nm to 50 nm, the ballistic drain transconductance, g_{ds} increases very slightly. As the channel length scales down to 50 nm the output transconductance, gds, however, rises significantly due to electrostatic gate effect. At

short channel length (10-40 nm) the drain transconductance becomes constant that helps to keep the constant cut-off frequency in short channel lengths.

6.2 Recommendations

This work can be extended in following ways:

(1) As graphene FETs suffer from low I_{on}/I_{off} ratio, opening of band gap in bilayer graphene has made graphene a viable replacement for semiconductors. Since the device physics of bilayer graphene transistors is still in embryonic stage, the knowledge of graphene and semiconductors can be extended to analyze the behavior of bilayer graphene and prospects in nano photonics and nano scale electronics.

(2) A band gap is opened in bilayer graphene by applying an electric field perpendicular to the layers that breaks the sublattice symmetry of the lattice.In addition to band gap opening, another electronic property that can be harnessed in design of logic transistors based on bilayer graphene is a pseudo spin degree of freedom associated with the electron-density difference between the two layer. A model for pseudo spin based bilayer graphene FETs can be developed.

(3) A preliminary 1D Poisson and Schrodinger analysis is used here. For better understanding of device physics 2-D analysis is essential. So our future plan is to analyze the whole work in 2-D structure.

(4) Here we have ignored the scattering effects including acoustic and phonon. We will include all the scattering effects further.

References

[1]   A. K. Geim and K. Novoselov, "The Rise of Graphene," *Nature Materials*, vol. 6, pp.183–191, 2007.[Online]. Available: http://dx.doi.org/10.1038/nmat1849.

[2]   A. S. Mayorov et al. Nano Lett., 11:2396-2399, (2011).

[3]   S. V. Morozov, K. S. Novoselov, M. I. Katsnelson, F. Schedin, D. C. Elias, J. A.Jaszczak, and A. K. Geim. Phys. Rev. Lett., 100:016602, (2008).

[4]   C. Lee, X. D. Wei, J. W. Kysar, and J. Hone. Science, 321:385-388, (2008).

[5]   F. Liu, P.M. Ming, and J. Li. Phys. Rev. B, 76:064120, (2007).

[6]   A. A. Balandin. Nat. Mater., 10:569-581, (2011).

[7]   R.R. Nair, P. Blake, A.N. Grigorenko, K.S. Novoselov, T.J. Booth, T. Stauber, N.M.R. Peres, and A.K. Geim. Science, 320:1308, (2008).

[8]   J. S. Bunch et al. Nano Lett., 8:2458-2462, (2008).

[9]   J. Moser, A. Barreiro, and A. Bachtold. Appl. Phys. Lett., 91:163513, (2007).

[10] D. C. Elias et al. Science, 323:610-613, (2009).

[11] K. P. Loh, Q. L. Bao, P. K. Ang, and J. X. Yang. J. Mater. Chem., 20:2277-2289, (2010).

[12] R. R. Nair et al. Small, 6:2877-2884, (2010).

[13] Y.M. Lin, C. Dimitrakopoulos, K.A. Jenkins, D.B. Farmer, A. Grill H.Y. Chiu and, and P. Avouris. Science, 327:662, (2010).

[14] K. Kim, J.Y. Choi, T. Kim, S.H. Cho, and H.J. Chung. Nature, 479:338-344, (2011).

[15] K. S. Novoselov, A. K. Geim, S. V. Morozov, D. Jiang, Y. Zhang, S. V. Dubonos, I. V. Grigorieva, and A. A. Firsov, "Electric Field Effect in Atomically Thin Carbon Films," *Science*,   vol.   306,   no.   5696,   pp.   666–669,   2004.OnlineAvailable: http://www.sciencemag.org/cgi/content/abstract/306/5696/666.

[16] A. H. Castro Neto, F. Guinea, N. M. R. Peres, K. S. Novoselov and A. K. Geim, "The electronic properties of graphene", Rev. Mod. Phys., vol. 81, no. 1, pp. 109–162, Jan 2009.

[17] A. K. Geim, K. S. Novoselov, "The rise of graphene", *Nature Materials*, vol. 6, pp. 183 - 191, 2007.

[18] J. Oostinga, H. Heersche, X. Liu, A. Morpurgo, and V. L.M.K., "Gate-induced insulating state in bilayer graphene devices", Nature Materials, vol. 7, pp. 151–157, 2008.

[19] S. K. Banerjee, L. F. Register, E. Tutuc, D. Basu, S. Kim, D. Reddy, and A. H. Mac-Donald, "Graphene for cmos and beyond cmos applications", Proceedings of the IEEE, vol. 98, no. 12, pp. 2032 –2046, December 2010.

[20] P. Avouris, "Graphene: Electronic and photonic properties and devices", Nano Letters, vol. 10, no. 11, pp. 4285–4294, 2010.

[21] A. K. Geim, "Graphene: Status and Prospects", Science, vol. 324, no. 5934, pp. 1530–1534, 2009.

[22] F. Schwierz, "Graphene transistors," *Nature Nanotechnology"*, vol. 5, pp. 487–496, 2010.

[23] K. S. Novoselov, A. K. Geim, "Two-dimensional gas of mass less Dirac fermions in graphene", *Nature* vol. 438, pp. 197-200, 2005.

[24] F. Schedin, A. K. Geim, "Detection of individual gas molecules adsorbed on graphene", *Nature Materials* vol. 6, pp. 652 – 655, 2007

[25]   Inanc Meric, Melinda Y. Han, Andrea F. Young, "Current saturation in zero-bandgap, top-gated graphene field-effect transistors", *NatureNanotechnology*, vol. 3, pp.654 – 659, 2008.

[26]   K.I. Bolotina, K.J. Sikesb, Z. Jianga,d, M. Klimac, G. Fudenberga, J. Honec, P. Kima, H.L, "Ultrahigh electron mobility in suspended graphene", *Solid State Communications* vol. 146, pp. 351–355, 2008.

[27]   N. M. R. Peres, "The Transport Properties of Graphene", J. Phys. Condens.Mater, vol. 21, Art.323201, 2009.

[28]   R S Shishir, D K Ferry, "Velocity saturation in intrinsic graphene", *Journal of Physics: Condensed Matter*, vol. 21, no. 34, 2009 .

[29]   Scott, B. W., Leburton, J., "High-field carrier velocity and current saturation in graphene field-effect transistors", *10th IEEE Conference on Nanotechnology (IEEE-NANO)*,pp. 655-658, 2010.

[30]   Balandin, A. A. et al. "Superior thermal conductivity of single-layer graphene", Nano Lett. 8, 902-907, 2008.

[31]   T.Fang, A. Konar, H. Xing, D. Jena, "Carrier statistics and quantum capacitance of graphene sheets and ribbons", Appl. Phys. Lett., vol. 91, Art. 092109, 2007.

[32]   S. Luryi, "Quantum Capacitance Device", Appl. Phys. Lett., vol. 53, no. 6, pp. 501-503, 1988.

[33]   S. A. Thiele, J. A. Schaefer, F. Schwierz, "Modeling of graphene metal-oxide-semiconductor field-effect transistors with gapless large-area graphene channels", *J. Appl. Phys.*vol. 107, pp. 094505, 2010.

[34]   Jilin Xia, Fang Chen, Jinghong Li, Nongjian Tao, "Measurement of the quantum capacitance of graphene", *Nature Nanotechnology*, vol. 4, pp. 505 – 509, 2009.

[35]   Ercag Pince, Coskun Kocabas, "Investigation of high frequency performance limit of graphene field effect transistors", *Appl. Phys. Lett.*, 97, 173106, 2010.

[36]   S. Thiele and F. Schwierz, "Modeling of the steady state characteristics of large-area graphene field-effect transistors", *J. Appl. Phys.*, vol. 110, pp. 034506-034506-7, 2011.

[37]   M. S. Lundstrom, R. W. Dutton, D. K. Ferry and K. Hess, "New Challenges and Directions", IEEE Transactions on Electron Devices, Special Issue on Computational Electronics:, edited by (2000).

[38]   C. P. Collier, E. W. Wong, M. Belohradsky, F. M. Raymo, J. F. Stoddart, P. J. Kuekes, R. S. Williams, and J. R. Heath, Science 285, 391 (1999); J. Chen, M. A. Reed, A. M. Rawlett, and J. M. Tour, Science 286, 1550 (1999).

[39]   R. Lake, G. Klimeck, R. C. Bowen, and D. Jovanovic, J. Appl. Phys. 81, 7845 (1997) and references therein.

[40]   Supriya Datta, "Superlattice and Microstructures" , vol.28, No. 4, 2000.

[41]   S. Datta, *Electronic Transport in Mesoscopic Systems* (Cambridge University Press, UK, 1997).

[42]   Y. Imry, *An Introduction to Mesoscopic Physics* (Oxford University Press, UK, 1997).

[43]   D. K. Ferry and S. M. Goodnick, *Transport in Nanostructures* (Cambridge University Press, 1997).

[44]   R. F. Pierret, *Advanced Semiconductor Fundamentals*, Modular Series on Solid State Devices, (Addison-Wesley) Vol. VI, p. 57.

[45]   Jyotsna Chauhan, Leitao Liu, Yang Lu,and Jing Guo: Appl. Phys.111 (2012) 094313.

[46]   Jyotsna Chauhan: Ph.D thesis University of Florida, Gainesville (2012).

[47]   I. Meric, M. Y. Han, A. F. Young: Nature Nanotechnology 3 (2008) 654.

[48]   J. Kedzierski, P.-L. Hsu, A. Reina, J. Kong, P. Healey, P. Wyatt, and C. Keast :IEEE Electron. Dev. Lett. 30, (2009) 745.

[49]   K. S. Novoselov, A. K. Geim: *Nature* 438 (2005) 197.

List of Publications

<u>International Conference:</u>

1. Md. Tawabur Rahman, Ashish Kumar Roy, Hossain Md. Abu Reza Bhuiyan, Md. Tajul Islam and Ashraful G. Bhuiyan "DC Characteristics of Dual Gated Large Area Graphene MOSFET," 1st International Conference on Electrical Information and Communication Technology (EICT 2013) 13-15 February 2014, Khulna-9203, Bangladesh.

<u>Peer Reviewed Journal:</u>

1. Md. Tawabur Rahman, Ashish Kumar Roy, Md. Shamim Sarker, Md. Tajul Islam, "AC Characteristics of a Dual Gate Large Area Graphene MOSFET," Global Journal of Researches in Engineering (USA), 2014.